Vibration-assisted decommissioning of a slip joint: Application to an offshore wind turbine

Cabboi, A.; Kamphuis, Thijs; van Veldhuizen, E.; Segeren, M.L.A.; Hendrikse, H.

DOI
10.1016/j.marstruc.2020.102931

Publication date
2021

Document Version
Final published version

Published in
Marine Structures

Marine Structures 76 (2021) 102931

Contents lists available at ScienceDirect

Marine Structures

journal homepage: www.elsevier.com/locate/marstruc

Vibration-assisted decommissioning of a slip joint: Application to an offshore wind turbine

Alessandro Cabboi [a,*], Thijs Kamphuis [b], Evert van Veldhuizen [a], Maxim Segeren [a], Hayo Hendrikse [a]

[a] Faculty of Civil Engineering and Geosciences, Delft University of Technology, Stevinweg 1, 2628CN Delft, NL, Netherlands
[b] Delft Offshore Turbine DOT B.V., Schieweg 15D, 2627AN Delft, NL, Netherlands

ARTICLE INFO

Keywords:
Jointed structures
Friction
Experimental modal analysis
Offshore structures
Shell structures

ABSTRACT

An alternative option to the traditional grouted joint for wind turbines is a direct steel-to-steel connection, also known as slip joint. In a recently published work, a proof of concept of a vibration-assisted installation and decommissioning technique of a slip joint was illustrated. Leveraging on the obtained results, the current study shows for the first time a decommissioning campaign carried out using a vibration-assisted technique applied on a prototype hydraulic wind turbine tower located in the North Sea, and connected to the monopile through a slip joint. The key aspect of the dismounting procedure is a priori knowledge of the resonance frequency clusters corresponding to the slip joint's cross-sectional modes. Therefore, field hammer tests and experimental modal analysis were carried out inside the wind turbine tower. The identified frequencies and mode shapes were then compared with numerical ones estimated by a finite element model of the investigated structure. The comparison showed that a set of frequency clusters can be directly selected from a detailed numerical model. The preparatory work of the slip joint decommissioning was then executed by installing electric shaker devices, based on the dynamic identification results, and hydraulic jacks mounted inside the wind turbine tower. A first decommissioning trial was carried out in May 2019, while the final decommissioning was performed in August 2019. After analysing the measurements of the hydraulic pressures, displacements and excitation frequencies during the decommissioning campaigns, the results showed that it is possible to disconnect the slip joint if, in combination to a vertical static force, one of the identified cross-sectional mode shapes is excited. The vibration-assisted decommissioning proved to be a successful technique to dismount the connection in a controlled and straightforward manner.

1. Introduction

1.1. Slip joint technology

One of the most common techniques to install a wind turbine tower on its corresponding monopile foundation is the grouted connection. Around 2009, the wind energy community started to observe a series of alarming consequences due to the fallacies of the governing design standards [1,2] concerning the grouted connection. The significantly high retrofitting costs motivated a joint effort between research groups and industry to pin down and understand the failure mechanisms [3–6], and concurrently propose

* Corresponding author.
E-mail address: A.Cabboi@tudelft.nl (A. Cabboi).

https://doi.org/10.1016/j.marstruc.2020.102931
Received 8 July 2020; Received in revised form 27 November 2020; Accepted 21 December 2020
Available online 6 January 2021

improved design options [7–13]. An alternative solution to the grouted connection consists of bolted flanges. The downside of the latter solution is that the installation [14] and maintenance phase [15,16] require special care and extra costs, in order to preserve the structural integrity of the connection. Note that the collapse of a wind turbine in 2015, located in Lemnhult (Sweden), was attributed to a loss of bolt tightness [17]. In 2003, the possibility of using the slip joint for offshore wind turbines was considered [18]. As already described in previous work [19,20], the slip joint technology is a valid alternative solution to overcome the design, maintenance and cost limits of the grouted and bolted flange connection. The idea behind a slip joint is rather intuitive and simple: a connection can be achieved by overlapping the bottom conical section of a wind turbine tower (or of the transition piece) on the top of the conical section of a monopile foundation, resulting in a substantial reduction of installation time. The load transfer between tower and foundation merely depends on the contact and frictional mechanism between the two overlapped conical surfaces.

The development and installation of a slip joint prototype for onshore use was promoted initially by DOT (Delft Offshore Turbine) and TUD (Delft University of Technology) within the R&D project SLJ (Onshore Slip Joint [21]). Recently, the aforementioned parties and other industrial partners (VanOord, TNO, SIF) extended the development of the slip joint technology for offshore purpose through the SJOR and SJOQ project (Slip Joint Offshore Research and Slip Joint Offshore Qualification, respectively). Within both projects, in September 2018, a 500 kW hydraulic DOT500 wind turbine and its corresponding tower were installed on top of a monopile by means of a slip joint (see Section 2 for further details). As part of the SJOQ project, the structural behaviour of the installed slip joint was monitored until its decommissioning between May and August 2019.

The current paper describes and focuses on the decommissioning of the 500 kW hydraulic DOT500 wind turbine, which was carried out by using a vibration-assisted technique in order to reduce the frictional resistance and consequently the force required to disconnect the slip joint. It should be mentioned that this slip joint decommissioning technique for wind turbine application is currently part of an ongoing EU patent application [22], jointly filed by DOT and TUD. The same technique was also extended for installation purpose of a slip joint, as already described in a recent published work [19]. The main difference between the vibration-assisted installation and decommissioning phase only relies on the application of a pushing (or pulling) force to lift up the upper tower, while in both phases the selected cross-sectional mode shapes would be excited. On a general note, whether the decommissioning is performed through a vibration-assisted technique or not has no significant effect on the technology readiness level of the slip joint. Note though, that this technique facilitates the slip joint disconnection for final decommissioning and for other applications such as seafastening. In general, the idea of exploiting vibration to reduce and alter friction forces is a rather intuitive strategy and the first systematic investigations started by the end of the ’60s of the last century. A short description of its state-of-the-art is provided in Section 1.2. However, it is worth anticipating that most of the studies found in literature are experimental ones, conducted by means of small laboratory test or “toy” rigs. Most of these experimental studies suggest a strong dependence on the characteristics of each test-rig, which often led to contradicting and substantially different outcomes and conclusions. As a result, there exists no convincing universally accepted physical interpretation which allows to explain the influence of deliberately applied vibration on the observed frictional force reduction.

1.2. State-of-the-art and research scope

The variation of the rheological properties of systems when excited by means of a vibratory load falls into the field of vibrorheology, according to the definition provided by Blekhman [23]. One of the branches of this field pursues the variation and possibly the reduction of the frictional force between two systems in contact by exploiting applied vibratory loads. In practice, it is quite common to witness friction reduction caused by applied oscillatory forces. The most intuitive example is provided by shaking tables that allow bodies at rest to walk off. Loosening of nuts and bolts can also be facilitated by applying a vibratory forcing. The list of applications can be quite extensive since jiggling an object that seems to be stuck tends often to be an efficient and practical strategy to get it loose. Despite the practical efficiency, a universally accepted physical interpretation of how static and kinetic friction forces change and react to externally applied vibration is still missing. A short review of friction reduction caused by oscillation applied normally to the contact surface is provided here. A more thorough review would have also included the case of an oscillatory force applied parallel to the sliding direction, however, the proposed slip joint decommissioning procedure [19] (also see Section 5) implies the installation of shakers pointing normal to the slip joint surface.

One of the earliest experiments aimed at investigating the effect of oscillatory forces on kinetic and static friction was carried out in the ’60s [24–26]. In these studies, it was experimentally shown that the estimates of friction coefficients can be significantly reduced (up to 80%) once an oscillatory force is acting normal to the sliding plane. However, no general law explaining the observed behaviour was proposed. Only at the beginning of the ’90s, a first analytical and numerical attempt started to shed some light on vibration-induced friction reduction. Hess and Soom [27–29] showed that a normal oscillation applied on top of a Hertzian contact leads to a reduction of contact deflection and consequently of the contact area. Assuming an adhesion theory of friction [30], and a driving frequency equal to the contact resonance with a normal oscillatory amplitude below that required to cause a temporary loss of contact, a friction force reduction around 10% can be achieved [27,29]. Tworzydlo and Becker [31] worked on a fairly similar model by assuming a non-linear normal interface compliance according to the Oden and Martins constitutive law of friction [32]. Their analysis revealed that the most sensitive parameters for friction reduction under applied vibration are the frequency of vibration, which has to be close to the contact resonance frequency, and a low interface damping. On the other hand, a high interface damping caused by micro-slip or wear debris, weakens the friction reduction effect induced by vibration. Notable recent work on modelling of friction reduction caused by applied normal oscillation was carried by Wetter and Popov [33]. Their study extended the models proposed by Tolstoi [26] and Oden and Martins [32] to investigate the spatial interconnection between the variation of normal and

(a) Picture of the DOT wind turbine.

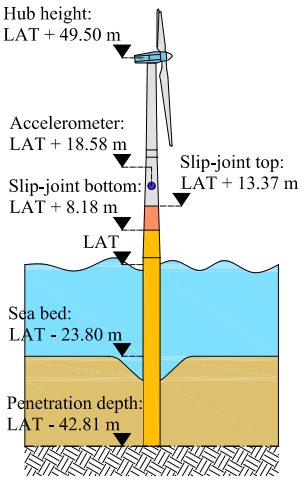

(b) Schematic layout of the structure.

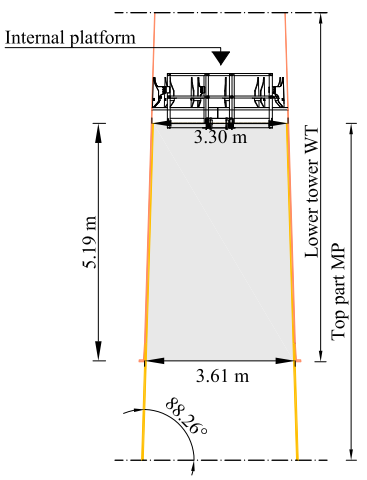

(c) Detailed drawing of the slip-joint.

Fig. 1. Overview of the investigated wind turbine and slip joint. The shaded grey area in Fig. 1(c) indicates the overlap of the slip joint. The abbreviation MP stands for monopile, while WT refers to wind turbine tower.

tangential forces and the friction reduction. The main conclusion is that the friction reduction predicted by their model is mainly caused by a "micro-walking" effect during which the normal oscillations plays a dominant role.

From an experimental point of view, it is worth mentioning the systematic testing carried out by Chowdhury and Helali [34,35] with a pin-on-disc rig. The effect of increasing forcing amplitude (10—200 μm) and frequency of vibration (0–500 Hz) on the coefficient of friction was investigated for different materials. The results showed that for mild steel pin on mild steel disc the frequency of vibration was the driving parameter for friction reduction (up to 60%), while for other disc materials the amplitude of vibration led to the biggest reduction rate (up to 60% for a rubber disc). It is interesting to note that during recent experiments carried out on a scaled slip joint made out of steel [19], the frequency of vibration showed to be the most sensitive parameter for friction reduction as well, while no particular influence of the vibration amplitude was observed. On the other hand, Teidelt et al. [36] showed that for steel on steel contact excited by a normal oscillation, the friction reduction is merely dependent on the amplitude of oscillation.

Within this context, the current work aims to show a unique application of the vibration-induced friction reduction technique [19] for the decommissioning of a large-scale structure, specifically a 500 kW hydraulic wind turbine mounted on a monopile foundation by means of a slip joint. To the best of the authors' knowledge, an attempt to use a deliberate oscillatory load to facilitate the disconnection between two structures of such size was never documented before. The description of the investigated structure and the development of a finite element (FE) model is reported in Sections 2 and 3, respectively. According to previous work [19], the key to successfully execute a vibration-assisted decommissioning of a slip joint lies in knowing in advance the frequencies of the first local circumferential mode shapes of the connection. Therefore, experimental modal analysis in loco of the slip joint was carried out to identify such modes. Section 4 presents the results of the dynamic identification process and a comparative study with the modal properties extracted from the developed FE model of the investigated structure. Given that the wind turbine tower mass is known to a sufficient degree and by assuming different and possible frictional regimes between the two conical surfaces in contact, a qualitative estimate of the required pushing (or pulling) force to disconnect the slip joint is provided in Section 5.1. Based on the results obtained in Sections 4 and 5.1, a decommissioning plan was laid out. Section 5.2 illustrates the decommissioning test plan and describes the positioning of the hydraulic jacks and electric shaker devices mounted at the base of the wind turbine tower. The wind turbine tower was bound for decommissioning in August 2019 and a preparatory test campaign was undertaken in May 2019. Finally, the experimental observations performed during two decommissioning campaigns are presented in Section 5.3. It is worth anticipating that the disconnection of the slip joint was successfully facilitated by an applied vibratory load while exciting a specific identified local mode of the connection. The entire decommissioning operation in August 2019 was also filmed. A short online video, see [37], provides the reader with a visual overview of the last decommissioning campaign.

2. Description of the full-scale wind turbine and slip joint

In September 2018, a prototype 500 kW hydraulic wind turbine was installed in the North Sea within the Princess Amalia Wind Farm, located 23 km from the Dutch coast. The lower tower of the wind turbine (WT) was directly connected to the monopile (MP) by means of a slip joint without the use of a transition piece. Fig. 1 provides a general overview of the investigated structure.

The total height of the investigated structure is about 92 m. The wall thickness of the curved steel plates forming the monopile and the wind turbine tower decreases with increasing height, from 65 mm to 10 mm. The overlapped area covered by the slip joint is

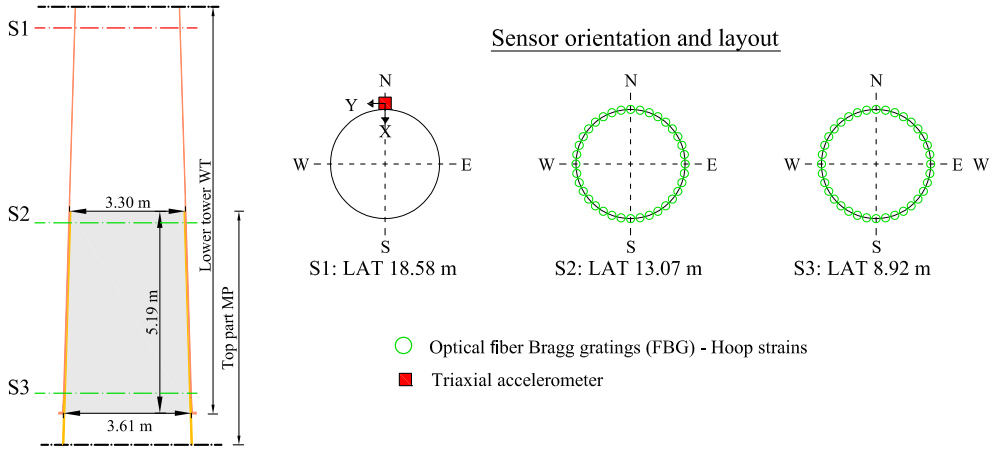

Fig. 2. Overview of the sensor layout: accelerometers and strain gauges.

indicated with a grey shading in Fig. 1(c). The total overlap after the slip joint was installed was about 5.19 m, including the initial settlement of the contact. It is worth mentioning that the measured overlap was very close to the target overlap estimated during the design phase (5.20 m) despite an initial monopile misalignment with the vertical direction. The target overlap was obtained by adopting design criteria discussed in previous research [20,21]. Such criteria are based on stress development caused by vertical and horizontal forces acting on the slip joint, following standard structural mechanic principles for vessel and cylindrical structures [38]. In addition, the ideal contact area was reduced by a factor that takes into account standard DNVGL fabrication tolerances [39] in order to avoid eventual restrictions on such tolerances.

The wall thickness of the top part of the monopile was 40 mm, while the thickness of the bottom part of the lower tower, which overlaps with the monopile, was 15 mm. The chosen cone angle was 88.26° respect to the horizontal plane. Fig. 1(c) also shows an internal platform mounted inside the lower tower, located slightly above the upper edge of the slip joint. The internal platform was the work space for the field hammer tests described in Section 4. The dead-weight acting on the slip joint included the mass of the nacelle (21.1 ton), the blades (3 × 2.1 ton), the nose cone (2 ton), the upper tower (14.1 ton), the lifting points of the tower (3 ton), the guide rail (1.3 ton), the external sky box platform (15.3 ton) and the lower tower (23.4 ton). The total mass triggering the frictional mechanism at the slip joint's interface is therefore around 86.5 ton.

As part of the SJOQ project, a long-term monitoring campaign was carried out to measure the structural behaviour of the slip joint for seven months (October 2018–May 2019). The data allowed to monitor the static and low-frequency dynamic behaviour of the slip joint under different operational and environmental conditions. Part of the static response was monitored through two horizontal arrays of optical fibre sensors measuring the circumferential strains (hoop strains) at a sampling frequency of 14 Hz, attached to the outer wall of the wind turbine tower (see the green dashed lines at level S2 and S3 in Fig. 2). For the latter, each cross-section was instrumented with 36 sensors. The dynamic response was recorded by a seismic triaxial ICP accelerometer, with a sensitivity of 1 V/g and a sampling frequency of 30 Hz, mounted at the lower part of the wind turbine tower (see Figs. 1(b) and 2, LAT 18.58 m).

This study will make limited use of the data provided by the aforementioned monitoring campaign, since a more detailed discussion about the strain and stress development within the slip joint during the installation phase and operational conditions will be the focus of future work. It suffices to say that during the monitoring period the slip joint settlements showed a tendency to stabilize over time. Note that the offshore structure under investigation was subject to severe winter storms, several wave slamming events and induced artificial loads triggered by multiple emergency-stop procedures of the turbine. Each significant load event triggered a settlement that rapidly converged to a stable level over time. Concurrently, the hoop strains measured during the aforementioned events stayed well below the yield limit. It is worth mentioning that despite the occurrence of settlements over time, no frequency variation of the first and second bending mode of the structure was observed.

3. Finite element model and global modes of the investigated structure

A finite element model of the whole investigated structure was developed in Abaqus FEA [40]. At this stage of the research, the scope of the presented FE model is neither to precisely match the experimental observations nor to perform any model updating or validation, but rather to back up and corroborate some of the experimental results shown in Section 4 with physical insights. The numerical model is based on 95895 linear quadrilateral stress/displacement shell elements with reduced integration and a large-strain formulation. The approximate global size of each element is about 100 mm. The total number of nodes is 96837. The geometry of the monopile and the wind turbine tower was retrieved from technical drawings, and the main variations of the different shell thickness from the monopile to the top part of the wind turbine tower were taken into account. The nacelle, the nose cone and the blades were modelled as a point mass with an estimated eccentricity located at the top part of the wind turbine. Other

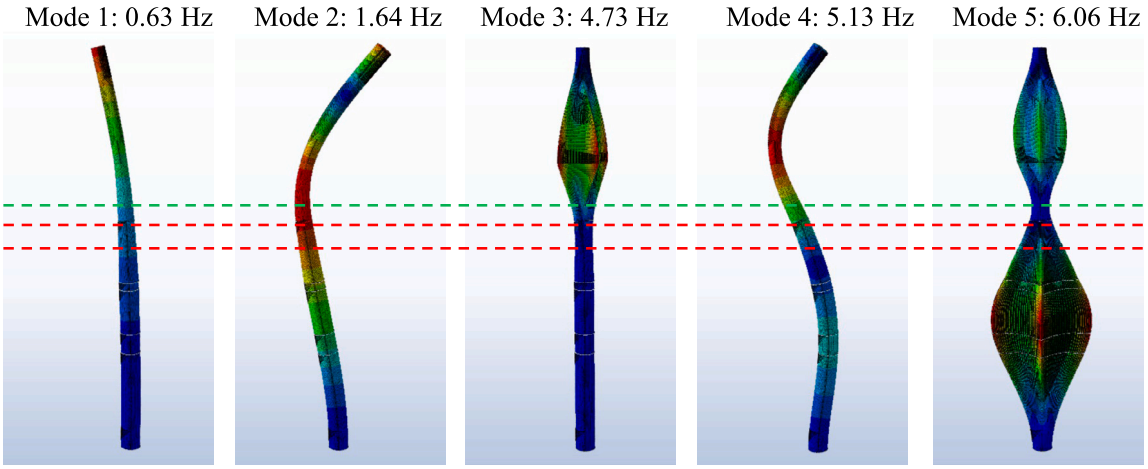

Fig. 3. First five mode shapes extracted from the FE model. The two horizontal dashed red lines define the location of the slip joint, while the green dashed line of the external platform. (For interpretation of the references to colour in this figure legend, the reader is referred to the web version of this article.)

non-structural elements such as the external platform the lifting points and the guide rail were modelled as structural distributed masses. The hydrodynamic mass was added as well, while the modelling of the foundation was simplified by assuming an encastre-like boundary condition at the level of the scour-depth, 10 m below the seabed level. The density of the steel material is assumed to be 8500 kg/m^3. The increased value approximately covers the density of steel, coating layers and other non-structural elements not directly modelled in the FE model. The selected Young's modulus for the structural steel is 210 GPa.

The contact interaction of the slip joint was modelled both in the tangential and normal direction of contact by assuming a surface-to-surface discretization [41]. For simplicity, complete contact of the two overlapping surfaces was assumed. The tangential contact formulation is based on Amonton–Coulomb's law by assuming a friction coefficient equal to 0.3, which approximately represents the friction force between coated steel elements. It is worth highlighting that the overall results provided in this Section and Section 4.3 are not influenced by the value of the friction coefficient. The friction formulation along the tangential direction is based on a stiffness (penalty) method, that allows a maximum elastic-slip equal to 0.5% of the total contact surface length. The pressure-overclosure relation along the direction normal to the contacting surfaces is modelled by assuming a "hard contact", meaning that the penetration of the slave surface into the master surface is minimized [42]. To control the small amount of penetration that may still occur, another stiffness (penalty) method is chosen to enforce the contact constraint by introducing a stiff linear contact spring [42]. These ideal assumptions revealed to be sufficient to simulate the main frequency bands location (up to 70 Hz) of the shell mode clusters nearby the slip joint, since the modal properties are computed based on a linear eigenvalue analysis performed on the mass and stiffness matrix obtained after a contact equilibrium (stick condition) is achieved. Note that if the final scope would be to investigate the actual stress and strain state of the contact interface during sliding or sticking conditions, the selected assumptions to model the contact interaction of the slip joint would need to be reviewed.

The final eigenvalue analysis was carried out in two steps. The first step aimed to initialize and settle the contact interaction. During this step, a small vertical displacement of 10 mm was applied to push down the wind-turbine tower. The displacement was applied through small increments in order to obtain a numerical convergence during the contact initialization and settlement of the slip joint. Subsequently, the second step consisted of running a modal analysis of the obtained equilibrium condition of the slip joint. Fig. 3 provides the natural frequencies and a graphical 3D view of the first five mode shapes obtained from the FE model.

The first estimated global modes from the FE model were then compared with the first identified resonance frequencies of the investigated structure. Fig. 4(a) shows an example of two time-series recorded along two directions, X and Y, orthogonal to each other and perpendicular to the axial direction of the tower. Both time-series exhibit a somehow random behaviour within the low-frequency band of the structure since the dynamic response is due to offshore ambient excitation. The accuracy of spectral analysis, applied to ambient-induced vibration data, depends on the length of the chosen time-window for the Fast Fourier Transform (fft) and the number of averages between each single fft result, allowing to minimize the noise content of the data. Therefore, the spectral analysis was performed using a total time length of 1400 s, in order to comply the rule-of-thumb recommendation of using a duration of the acquired time-series ranging between 1000 and 2000 times the fundamental period of the structure [43] to obtain accurate estimates of the modal parameters. The corresponding cross-spectrum, estimated between both directions, is shown in Fig. 4(b). The identified resonance frequencies are marked with a red dashed line. Two clear resonance peaks can be detected approximately at 0.605 Hz and 1.42 Hz, most likely representing the first two bending modes of the tower. Further smaller peaks are visible at 5.24 Hz and 5.65 Hz and a scattered cluster of peaks is also visible between 4.08 Hz and 4.3 Hz. Since it is not possible to retrieve mode shape information from a single accelerometer data set, the origin of these peaks and cluster is not entirely clear.

The natural frequencies obtained from the FE model are plotted in Fig. 4(b) with a dashed black line. The first simulated bending mode matches the experimental one quite closely, while the second bending mode seems to differ about 13%. As mentioned above,

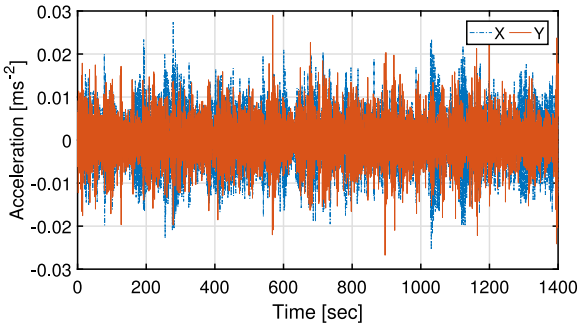

(a) Recorded acceleration along the the X-Y horizontal plane. Both time-series refer to the following date and time: 08/12/2018 - 04:00.

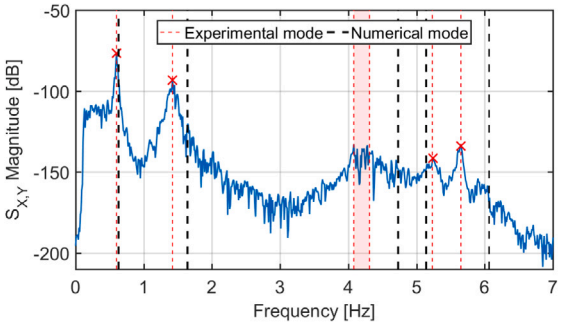

(b) Cross-spectral density between the acceleration of the X and Y direction.

Fig. 4. Low-frequency dynamics of the investigated structure.

the origin of the modes between 4 Hz and 6.1 Hz remains unclear. At the same time, the FE modal analysis showed the occurrence of three further natural frequencies exactly within the same frequency range. The mismatch between the peaks exhibited by the cross-spectrum and the simulated natural frequencies is quite evident. The observed discrepancy for these global modes can be caused by simplified modelling assumptions, especially concerning the connection and load transfer between the external platform and the wind-turbine tower. Note that the platform's mass was about 15 ton and could potentially induce localized modes on the structure nearby the platform. Further modelling simplifications such as the omission of both soil–structure interaction and presence of marine growth and the simplified mass distribution of the rotor–nacelle–blade assembly could also play a relevant role. However, for the current research objective, a correct match between the first global modes was not necessary. The main interest lies in the local mode shapes at higher frequencies nearby the top part of the slip joint, as discussed in Section 4, and in cross-checking on whether or not the nodal pattern sequence of the experimental circumferential modes is correctly identified.

4. Hammer tests and modal identification

4.1. Description of testing program and sensor layout

In a previous study [19] it was shown that additional settlements between two overlapping cones mimicking a slip joint installation procedure can be achieved through vibration-induced friction reduction. Similarly, the detachment of both cones was facilitated by the same principle. The key point of the procedure turned out to be the deliberate excitation of the resonance frequency of the system while a compressing or pulling load is applied. Therefore, in order to apply the proposed technique for the decommissioning phase, an experimental modal analysis campaign was carried out on the prototype hydraulic wind turbine installed within the Princess Amalia Wind farm, to identify the local mode shapes of the full-scale slip joint. The modal properties identified from the dynamic tests were then used to plan the decommissioning campaign described in Section 5.2.

The dynamic test setup is shown in Fig. 5. In total, 15 mono-axial Bruël & Kjær DeltaTron accelerometers were used. Each accelerometer, model 4514, has a sensitivity of 50 mV/g and a linear frequency response between 5–500 Hz. Considering the low sensitivity of the available sensors, it is worth anticipating that shell modes at frequencies lower than 20 Hz were not observable. An example of such missing modes is the first shell breathing mode, which was expected to occur around 12.5 Hz, according to the FE modal analysis. Given the sensors' constraint, the frequency of interest for the purpose of decommissioning shifted between 20–80 Hz. Besides the sensitivity of the sensors, the latter band was also a limitation given by the operational regime of the available electric shakers used for the decommissioning test, described in Sections 5.2 and 5.3 . The excitation impulses were provided by an instrumented ICP impact hammer with a hard plastic tip (model type 086D50), and the data acquisition system was a multi-channel PAK MKII purchased from Müller-BBM. The impact and sensing levels referred to different cross-sections as shown in Fig. 5(a). Four impact locations were chosen in Level 1, labelled as H1c1, H2c1, H1c2 and H2c2 and displayed with a black cross in the top view of Fig. 5(a). On the other hand, the dynamic responses were recorded at three different levels, from Level 2 to Level 4. Fig. 5(b) visualizes three marked points referring to the three different sensing levels on the internal side of the slip joint. For each Level, two tests were carried out by first mounting 15 accelerometers on half circumference labelled as c1 (green circles Fig. 5(a)) and subsequently moving the same sensors on the second half of the circumference labelled as c2 (blue circles Fig. 5(a)). The red circle in Fig. 5(a) defines the reference sensor between both tests. For each test, five impacts were provided at each impact location for a total number of hits equal to 20.

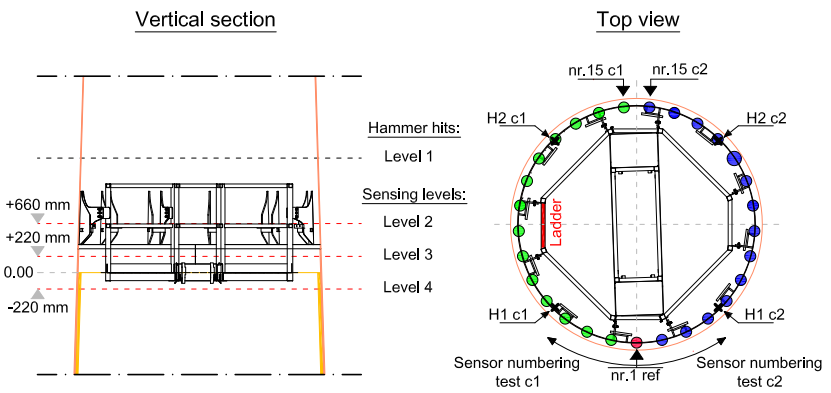

(a) Vertical section and top view of the sensor layout and hitting locations. The green and blue circles refer to the sensing points, while the black crosses define the hitting locations.

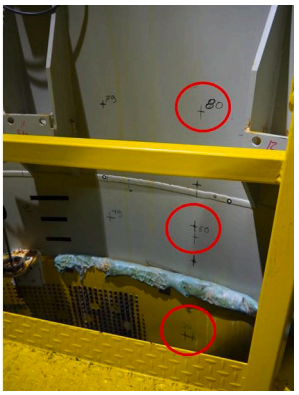

(b) Picture of the slip joint: the red circles refer to three sensing sections along the vertical direction.

Fig. 5. Overview of hammer test and sensing layout.

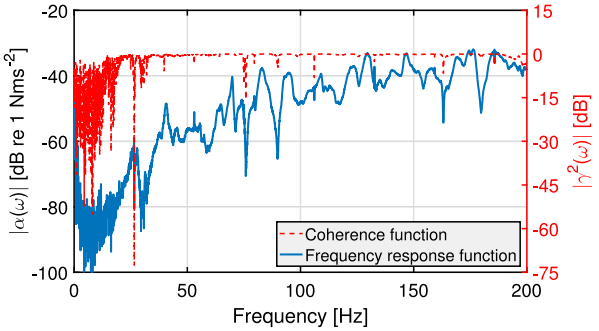

(a) Transfer function (blue line) and coherence function (red dashed line) between the measured input the dynamic response referred to sensor nr.1.

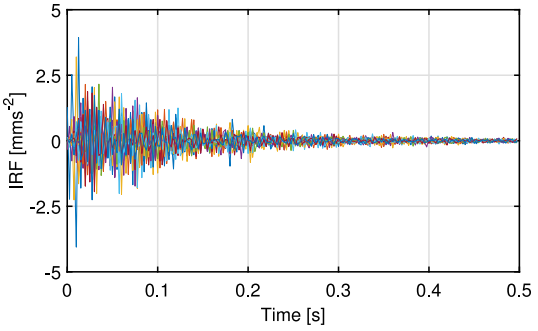

(b) 15 impulse response functions (IRFs) estimated from the corresponding transfer functions.

Fig. 6. Transfer function and impulse response functions estimated from dynamic responses at Level 2 during test c1 with reference to the input location H1c1.

4.2. Dynamic identification method

The dynamic responses were recorded with a frequency sampling of 400 Hz, and each measurement had a duration of 5 s, which were later zero-padded to 10 s. The time-series length leads to a frequency resolution of 0.1 Hz, enough to capture the main local resonance frequencies of the slip joint. Before processing the data, each measurement was projected onto the horizontal plane, considering the inclination of the slip joint cone. The H_1 estimator [44] was then used to compute the frequency response functions (FRFs) by averaging over five impacts and their corresponding free decay structural responses. A linearity check of each FRF was also performed by inspecting its corresponding coherence function. Fig. 6(a) shows an example of such estimates. As mentioned above, the dynamic response below 20 Hz was not clearly observable given the low sensitivity of the accelerometers.

Once all the FRFs were estimated, the inverse Fourier transform is applied in order to retrieve the corresponding impulse response functions (IRFs), see Fig. 6(b) for 15 estimated IRFs. Natural frequencies and mode shapes were then identified by applying an automated version of the Eigensystem Realization Algorithm (ERA) [45] on the estimated IRFs. The ERA method takes advantage of the time domain description of free dynamic responses provided by the Markov parameters which reads as follows:

$$\mathbf{Y}_{(k)} = \mathbf{C}\mathbf{A}^{k-1}\mathbf{B} \tag{1}$$

where $\mathbf{Y}_{(k)}$ is a p-dimensional vector containing the dynamic responses (IRFs) where k is a positive integer, $\mathbf{C}$ is the $p \times n$ output matrix with n defining the order of the system, $\mathbf{A}$ is the $n \times n$ dynamic system matrix and $\mathbf{B}$ is the $n \times m$ input matrix where m defines the number of inputs. The target of the identification algorithm is to estimate matrix $\mathbf{A}$ provided $\mathbf{Y}_{(k)}$ is given. The algorithm starts by gathering the measured responses $\mathbf{Y}_{(k)}$ in a generalized $rm \times rp$ Hankel matrix $\mathbf{H}_{(k)}$, where r and s are arbitrary chosen integers that correspond to a time lag of the recorded signal. For the current application r and s are assumed to be equal. According to

Eq. (1), the Hankel matrix is equivalent to the following matrix product

$$\mathbf{H}_{(k)} = \begin{bmatrix} \mathbf{C} \\ \mathbf{CA} \\ \mathbf{CA}^2 \\ \dots \\ \mathbf{CA}^r \end{bmatrix} \begin{bmatrix} \mathbf{B} & \mathbf{AB} & \mathbf{A}^2\mathbf{B} & \dots & \mathbf{A}^s\mathbf{B} \end{bmatrix} = \mathbf{\Gamma\Lambda} \tag{2}$$

where $\mathbf{\Gamma}$ and $\mathbf{\Lambda}$ are the observability and controllability matrix, respectively, which can be obtained by performing a singular value decomposition (SVD) of $\mathbf{H}_{(k)}$

$$\mathbf{H}_{(k)} = \mathbf{USV}^T. \tag{3}$$

Matrices $\mathbf{U}$ and $\mathbf{V}$ contain the singular orthonormal vectors and $\mathbf{S}$ the nonnegative singular values. The observability and controllability matrices can then be estimated as follows:

$$\hat{\mathbf{\Gamma}} = \mathbf{U}_n\sqrt{\mathbf{S}_n} \qquad \hat{\mathbf{\Lambda}} = \sqrt{\mathbf{S}_n}\mathbf{V}_n^T. \tag{4}$$

The subscript n defines the chosen model order that corresponds to the number of selected singular vectors and values. However, due to the ill-posed nature of the inverse problem, the decomposition defined in Eq. (2) is not unique. Therefore, in order to estimate the system matrix $\mathbf{A}$, a time-shifted Hankel matrix $\mathbf{H}_{(k+1)}$ is necessary which leads to the following relation:

$$\hat{\mathbf{A}} = \hat{\mathbf{\Gamma}}^{+}\mathbf{H}_{(k+1)}\hat{\mathbf{\Lambda}}^{+} \tag{5}$$

where the superscript $^+$ indicates the pseudo-inverse of the estimated matrices. Once the system matrix $\mathbf{A}$ is known, the natural frequencies and mode shapes can be retrieved by an eigenvalue decomposition of $\hat{\mathbf{A}}$. Note that one of the key steps of the identification algorithm is the choice of a model order n in Eq. (4). This step is tackled by selecting a possible range of model orders and taking advantage of stabilization diagrams that allow to visualize the convergence of identified modal properties for different model orders. The check of such convergence is performed in an automated way by using a clustering algorithm [46]. Identified poles which have a similar frequency and mode shape are merged in one single cluster. The similarity index used to form the clusters is defined as

$$d = \frac{|f_{ref} - f|}{f_{ref}} + 1 - MAC \tag{6}$$

where f_{ref} is a chosen reference value corresponding to the "seed" of the cluster, f is the frequency, and the MAC (Modal Assurance Criterion) is a similarity index for estimated mode shapes. A MAC value equal to 1 indicates that two mode shapes are consistent between each other, while a MAC value of 0 is typically observed between two orthogonal mode shapes. For the current work, a threshold of d=0.01 was defined. The obtained stabilization diagrams with corresponding modal clustering are shown in Section 4.3.

4.3. Identified local shell modes and comparison with the FE model

As illustrated in Fig. 5, the dynamic response was measured at three different levels. The dynamic identification method was then applied on each set of measurements referring to one level and covering a full circumference. For each run of the ERA algorithm, the number of selected output channels p was 30 and the input locations m corresponded to 4×2. The model order ranged from 100 to 300 with an increasing step of 2, while the Hankel matrix was built using two lag values, r and s, equal to 300. A visual summary of the results obtained by the identification algorithm is shown in Fig. 7 for each instrumented level by means of stabilization diagrams. For the sake of clarity, the vertical alignments of red dots identify the stable system poles that correspond to the resonance frequencies of the structure. A cross-check of the ERA results was performed by applying an SVD on the frequency response function matrix for each set of measurements. The latter technique, also known as Complex Mode Indicator Function (CMIF) [47], enables to plot the first singular values of the SVD results for each frequency line. The peaks of such plot clearly show the correspondence between resonance peaks and stable system poles.

Fig. 7 highlights that the data collected at Level 2 and 3 are characterized by a richer dynamic response compared to the measurements performed at Level 4. The reason for that is due to the shorter distance between the excitation points (Level 1 in Fig. 5(a)) and the sensors located at Level 2 and 3 compared to the sensing points at Level 4. In addition, between Level 4 and 3 there was a significant change in stiffness caused by the variation of the cylinder thickness from 15 mm (Level 3) to 55 mm (Level 4). On top of that, the slip joint at Level 4 introduced an additional source of dissipation which tended to dampen the induced energy by the hammer hits performed at Level 1.

In general, all the stabilization diagrams in Fig. 7 exhibit a phenomenon known as frequency splitting [48]. The phenomenon can be detected by the occurrence of two nearby vertical red lines around a resonance peak. For example, in Fig. 7(a), the frequency splitting is observable around a frequency of 40 Hz, 53 Hz, 64 Hz, 70 Hz and 75 Hz. This phenomenon is caused by a slight deviation from a condition of axial symmetry of the structure. Note that if the axial symmetry of a cylinder remains intact, the corresponding circumferential vibration modes occur in degenerate eigenpairs at the same natural frequency. Such eigenpairs are orthogonal between each other and have an indeterminate angular location around the axis of symmetry. On the other hand, a break of axial symmetry, which mimics the realistic conditions of the investigated structure, eliminates the angular indeterminacy and causes a small difference in terms of frequency between the previously mentioned eigenpair [49]. However, for the practical

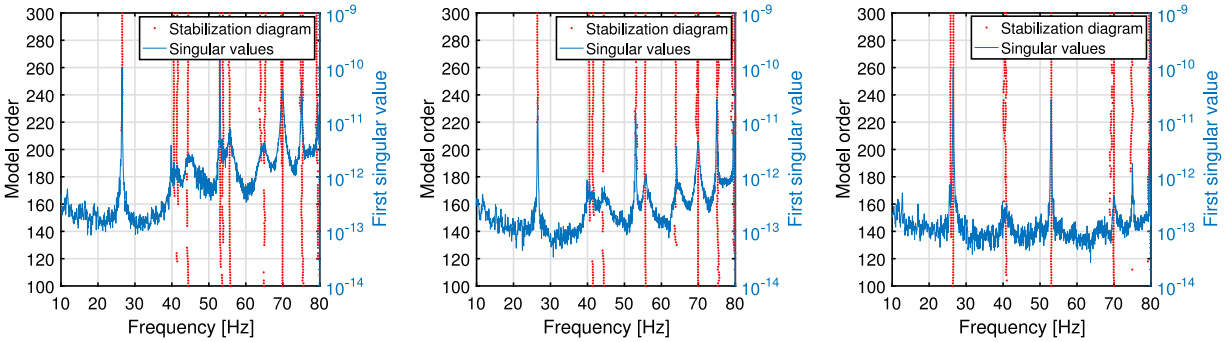

(a) Level 2. (b) Level 3. (c) Level 4.

Fig. 7. Stabilization diagrams (vertical dotted red lines) and estimated first singular values of the SVD (continuous blue line) performed on the cross-spectral density matrix. (For interpretation of the references to colour in this figure legend, the reader is referred to the web version of this article.)

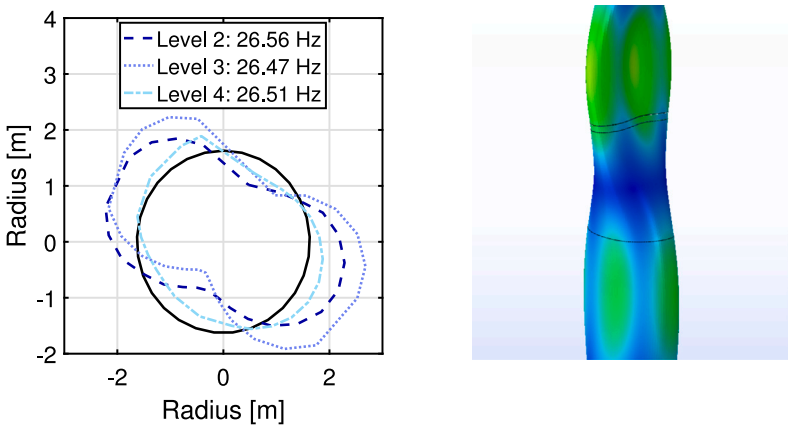

(a) Experimental modes (b) FEM mode: 26.44 Hz

Fig. 8. Comparison between experimental and FEM mode shapes for the resonance peak around 26.5 Hz.

purpose of this investigation, the quantification of the frequency splitting is not relevant and the main focus is centred around the identified resonance peaks. Each monitored cross-section shared five common resonance peaks around 26 Hz, 40 Hz, 53 Hz, 70 Hz and 75 Hz, while the resonance peak at 64 Hz seemed to be identifiable only at Level 2 and 3.

The mode shape patterns of the identified resonance frequencies are shown in Figs. 8–11. For each experimental mode shape, the corresponding numerical mode computed by the FE model described in Section 3 is shown. The plotted numerical mode shapes refer to the region around the slip joint confined by the upper and bottom black circumferential lines indicated in each FEM mode plot. Note that between experimental and numerical mode, only a qualitative comparison is possible, since to quantitatively assess the consistency between both modes more cross-sections need to be instrumented. From a qualitative perspective, there is a fairly good match between identified and computed mode shapes, except for the identified mode shape around 64 Hz, not illustrated in the aforementioned plots.

The vibrational mode shape of the first identified resonance frequency, shown in Fig. 8(a), is characterized by a circumferential nodal pattern index N=2, where N indicates the number of waves around the circumference. Figs. 9–11 show a nodal pattern index N equal to 3, 4 and 5, respectively. Previously, it was mentioned that the data collected at Level 4 seemed to be characterized by a lower dynamic content. This observation can also be corroborated by inspecting the mode shapes computed by means of the FE model. In fact, Level 4 refers to a cross-section right below the starting point of the slip joint, which often approaches a nodal circumferential line. This occurs for all the selected modes except for the mode at 44.07 Hz. In general, all the mode shapes identified from the data collected at Level 4 are more distorted, exhibiting a lower modal amplitude compared to the mode shapes of Level 2 and 3.

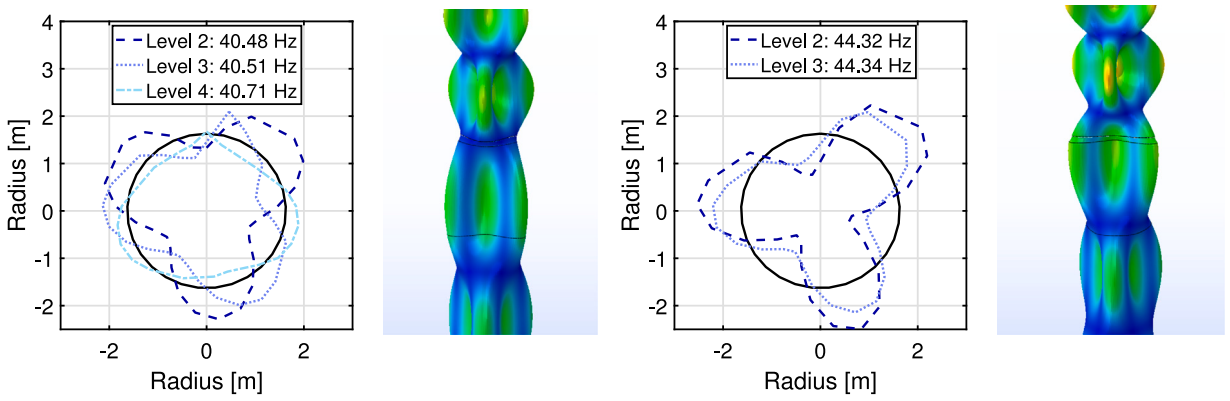

(a) Experimental modes (b) FEM mode: 40.92 Hz (c) Experimental modes (d) FEM mode: 44.07 Hz

Fig. 9. Comparison between experimental and FEM mode shapes for the resonance peaks around 40.5 Hz and 44.3 Hz.

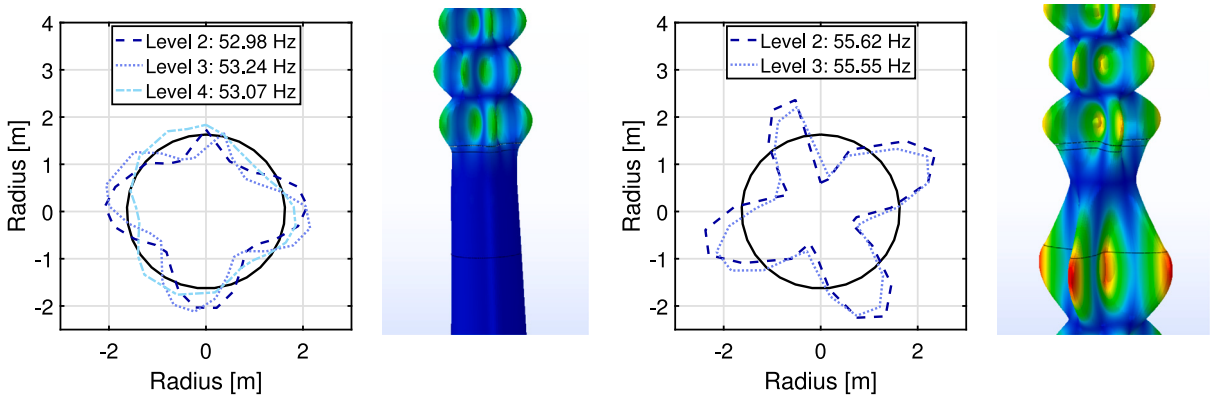

(a) Experimental modes (b) FEM mode: 53.30 Hz (c) Experimental modes (d) FEM mode: 56.48 Hz

Fig. 10. Comparison between experimental and FEM mode shapes for the resonance peaks around 53.3 Hz and 55.6 Hz.

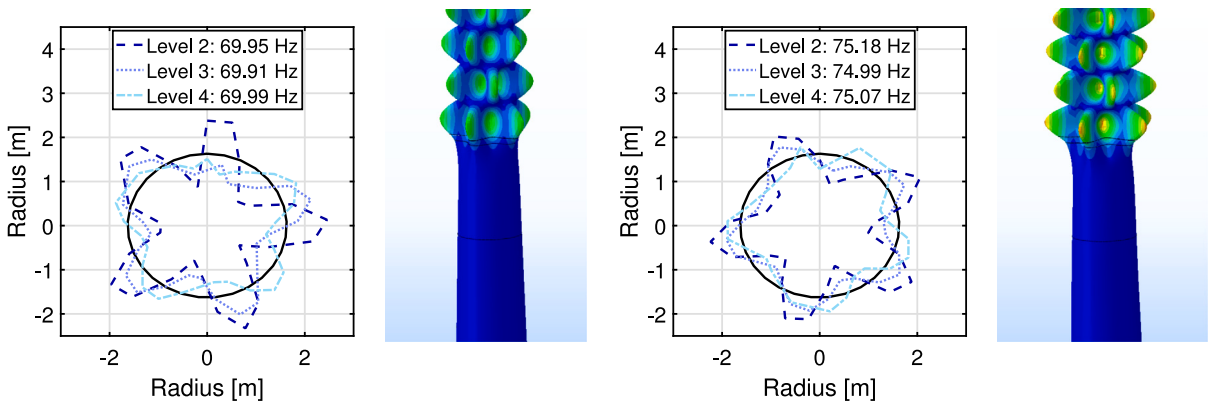

(a) Experimental modes (b) FEM mode: 70.98 Hz (c) Experimental modes (d) FEM mode: 78.13 Hz

Fig. 11. Comparison between experimental and FEM mode shapes for the resonance peaks around 69.95 Hz and 75.0 Hz.

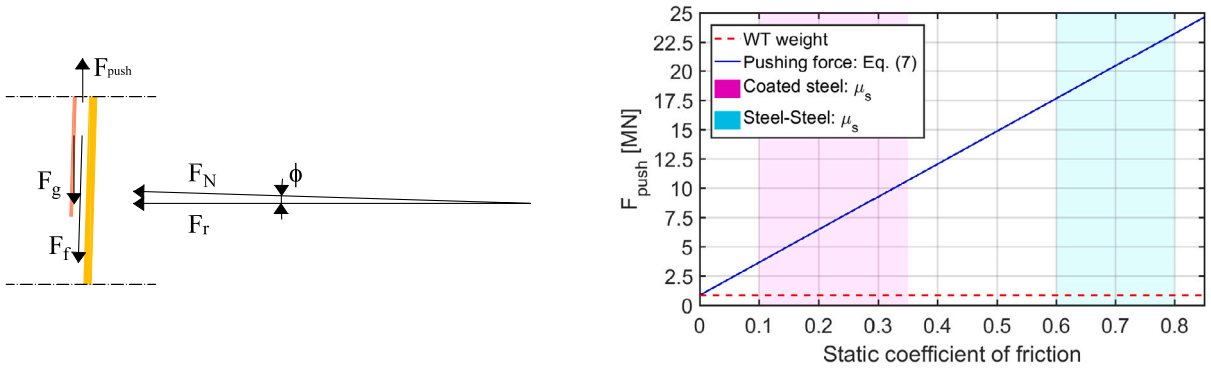

(a) Free body diagram of the slip joint's static forces (b) Estimated pushing forces.

Fig. 12. Free body diagram and estimated pushing forces according to Eq. (7). The shaded patches delimit the two selected friction regimes.

5. Decommissioning of the slip joint

5.1. Estimated pushing force to disconnect the slip joint

In this section, an estimate for the required force to disconnect the slip joint without the use of a vibration-induced friction reduction technique is presented. For the sake of clarity, the force is defined as a pushing force, since the decommissioning was carried out by means of hydraulic jacks (see Sections 5.2 and 5.3) mounted at the top part of the slip joint. A qualitative estimate of the pushing force can be obtained by imposing the static equilibrium of the forces acting along the vertical z-direction as shown in Fig. 12(a). The required pushing force F_{push} is

$$F_{push} = F_g + \frac{F_g \mu_s}{\tan \phi} \tag{7}$$

where F_g stands for the weight, μ_s is the Amonton–Coulomb's coefficient of static friction and ϕ is the cone angle. The weight of the wind turbine tower is approximately equal to 849 kN, while the cone angle ϕ respect to the vertical axis is equal to 1.74°. Note that by assuming the Amonton–Coulomb's friction law, the dependency between static friction force and contact area is neglected.

For the static friction coefficient, two different ranges were assumed. The first range refers to typical friction coefficients for mild steel on mild steel contact. The latter case assumes that the coating layer could undergo abrasion and wear during micro-slip motions of the slip joint caused by environmental and operational loads. According to Rabinowicz [50] and assuming that both materials have high metallurgical compatibility, the range of friction coefficient μ_s could be assumed between 0.6 and 0.8 (see [50], Table 4.3), keeping in mind that a typical value found in literature is 0.74 (see [51], Table 4.5). The second range refers to possible friction coefficients between two coated steel surfaces. It is known that the presence of the coating layer significantly reduces the friction coefficient between the two surfaces in contact. The external coating layer applied on the monopile's surface consisted of a primary internal epoxy-based layer (Sika-Cor SW 501) and a thinner external film made of an acrylic-polyurethane material (Permacor 2230 VHS). The internal layer of the wind turbine tower was made of a polyamide and epoxy-based paint (Hempadur Mastic 45880). Finding an accurate value of μ_s able to characterize the frictional force between the aforementioned coatings is not straightforward without performing an ad-hoc friction test. Such values strongly depend on the surface finish, the coating's material properties, the applied load, the contact configuration, the temperature, the contamination between the surfaces in contact and the eventual level of lubrication (e.g. level of humidity in an offshore environment). A first reasonable guess can be provided by looking up the μ_s values reported in Rabinonwicz's book (see Table 4.4 in [50]). The possible range of static friction coefficient between two non-metals (that are not identical) can be assumed to lie between 0.1 and 0.35. Based on a tribological study performed on steel samples combined with coatings typically employed in offshore applications [52], a slightly more narrow range, 0.2–0.35, was found. However, it is worth highlighting that the presence of the two coating layer may not be the only reason for a drastic friction reduction from 0.6–0.8 (typical μ_s values for steel on steel) to a possible 0.1–0.35 range. Tribological studies carried out on shrink-fit connections [53] and other structural joints [54], showed a significant decrease in the coefficient of friction with increased normal pressure. Recent studies showed that a typical μ_s for a shrink-fit joint characterized by high contact pressures ranges between 0.1 and 0.2 [55,56].

After substituting the input parameters in Eq. (7), a possible range of the required pushing forces to dismount the slip joint is shown in Fig. 12(b). It is worth noting that compared to the weight of the wind turbine tower (0.849 MN), the additional vertical force component generated by the frictional forces can reach values between 2.8 to 22 MN. In order to guarantee a safe and quick decommissioning of the slip joint through a pushing force, it is clear from Fig. 12(b) that a technique able to trigger a reduction of such contact forces is needed. The pushing force values presented in Fig. 12(b) are used as reference values and compared to the pushing forces measured during the decommissioning campaign described in Sections 5.2 and 5.3.

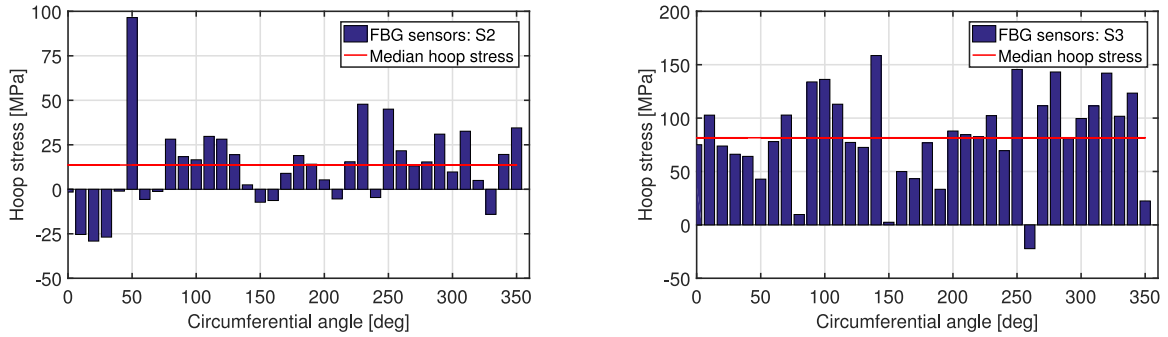

(a) Hoop stress estimated from FBG sensors at level S2, see Fig. 2. (b) Hoop stress estimated from FBG sensors at level S3, see Fig. 2.

Fig. 13. Estimation of averaged hoop stresses for each FBG sensor, 1 h before the decommissioning test on May 2019. The red line in both figures indicates the median value computed for each array of sensors.

Even though a detailed discussion about the strain and stress distribution over the slip joint and its evolution over time falls outside the scope of this paper, a qualitative validation of the range of values obtained from Eq. (7) can be carried out by inspecting the averaged hoop stresses estimated from the collected circumferential strain gauge data described in Section 2. Fig. 13 shows a snapshot of mean hoop stresses estimated from the last record of strain data, right before the first decommissioning test, referred to the 24th of May 2019 and collected between 23:00–0:00 h. The blue bars indicate a mean value for each sensor, while the red horizontal line refers to the global median value representing an equivalent uniform stress for the entire array of sensors. The observed discrepancy between the two median values suggests a possible non-uniform contact development over the overlapped area, while the major scatteredness observed in Fig. 13(a) is mainly caused by the low strain values measured at top of the slip joint approaching the noise level of the FBG sensors. On the other hand, the high value observed for the sensor positioned at an angle of 50° in Fig. 13(a) can most likely be considered as an outlier. Fig. 13(b) shows a more "uniform" distribution of the hoop stress over cross-section S3. Both figures seem to suggest that the contact between the two conical surfaces increasingly developed from the top to the bottom of the slip joint.

To make use of the aforementioned data, Eq. (7) can be rewritten in terms of the hoop stress in a back-of-the-envelope fashion, as originally shown in a previous study [20] but fully reported below for the sake of clarity. As illustrated in Fig. 12(a), the normal force acting on the slip joint's interface generates a radial force component F_r

$$F_r = F_N \cos\phi. \tag{8}$$

Assuming a perfect fit and overlap between the two cones in contact, the radial force F_r leads to a uniform pressure p which reads as

$$p = \frac{F_r}{hD\pi} \tag{9}$$

where h is the height of the overlap between the two cones and D is the diameter of a specific cross-section. The action of the uniform internal pressure p generates hoop stresses [38] in the cylindrical shell thickness t, given by

$$\sigma_h = \frac{pD}{2t} \tag{10}$$

which are assumed to be uniformly distributed over the thickness of the shell. After few substitutions and re-arrangements, Eq. (7) can be rewritten as

$$F_{push} = F_g + \frac{F_g \mu_s}{\tan\phi} = \sigma_h \; 2 \; t \; h \; \pi \; (\tan\phi + \mu_s) \tag{11}$$

where the first term of the right-hand side of Eq. (11) is linked to the weight of the wind turbine tower F_g, while the second term covers the generated friction force by the slip joint. Based on Eq. (11), the hoop stress reads as

$$\sigma_h = \frac{F_{push}}{2 \; t \; h \; \pi \; [\tan\phi + \mu_s]}. \tag{12}$$

By recalling that the order of magnitude of μ_s could be between 0.1–0.35 and that $\tan\phi$ is equal to 0.03, it seems obvious that one of the two factors that influence mostly the measured hoop stresses is the uncertainty of the coefficient of friction. On top of that, the effective value of h, which is directly linked to the real contact area, is also unknown and has a significant effect on the computed stresses. However, a possible value of the hoop stress can be inferred by assuming that F_g is known to a sufficient degree. In fact, according to Eq. (11), the hoop stress σ_h can also be rewritten as

$$\sigma_h = \frac{F_g}{2 \; t \; h \; \pi \; \tan\phi}. \tag{13}$$

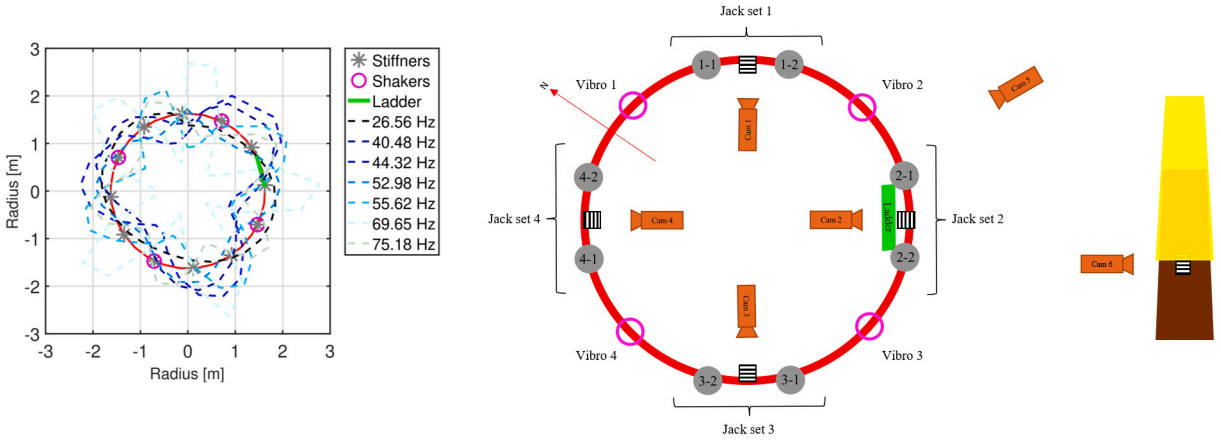

Fig. 14. Identified resonance modes (left) and schematic overview of installed decommissioning equipment (right).

According to Eq. (13) and assuming h equal to 5.19 m, σ_h turns out to be 57 MPa, which lies in between the two boundaries identified by the estimated median values shown in Fig. 13. The deviation between the higher median value (81.59 MPa) computed in Fig. 13(b) and the estimated one (57 MPa), could be explained by a possible variability of the frictional interaction between the two surface's in contact and/or due to a reduction of the contact area. So far, we assumed that the overlapped area between the two conical surfaces is entirely in contact. However, assuming the estimated median value, 81.59 MPa, to be representative of the hoop stress distribution at the bottom of the slip joint, an effective overlap h_{eff} equal to 3.63 m can be estimated from Eq. (13). The computed effective overlap constitutes 70% of the apparent measured overlap h. It is worth noting at this stage, that preliminary research carried out by DOT and TU Delft [57] on the contact area development between a slip joint, highlighted a 34% of contact area reduction (with 95% confidence interval between 23% and 51%). The latter estimate was performed using a continuous-heating thermographic point measurement method applied on a slip joint of a decommissioned onshore wind turbine.

5.2. Decommissioning setup and plan

5.2.1. Description of the decommissioning equipment

For practical reasons, carefully selected off-the-shelf components were used for the decommissioning. The pushing force was applied by using hydraulic jacks, type Hi-Force HSS-5013. The jacks had an individual maximum capacity of F_{jack}=491 kN with an effective cylinder area of A_{eff}=7130 mm^2, and a maximum stroke of l_{jack}=330 mm. Eight jacks were connected to the wind turbine tower wall by bolting them to purpose-built stiffeners. This secured the hydraulic jacks to the tower wall of the wind turbine while allowing them to introduce the pushing force on the top part of the monopile. The oscillatory loads on the wind turbine tower wall were introduced by means of four external electric shakers, type Netter NEG 501800, installed on the remaining four stiffeners. The external electric shakers had a rated power of 1 kW and were able to operate from f_{ex}=16.8 Hz to 80 Hz, with an exponentially increasing dynamic shaking force of F_{ex}=0.78 kN to 17.67 kN. The location around the tower circumference and frequency specifications of the electric shakers were chosen by taking into account the analysis performed in Section 4.3 and by keeping in mind a desirable uniform distribution of the hydraulic jacks. In relation to the modal analysis, the target in choosing the shaker locations was to avoid the nodal points of the identified circumferential modes, as much as possible. The selected sensor layout is illustrated on the left in Fig. 14.

All the equipment was installed at the monopile and wind turbine tower interface, accessible via the internal platform, see Fig. 1(c). A picture of an installed electric shaker and hydraulic jack and a drawing of an installed jack's working principle can be observed in Fig. 15. Additionally, six video cameras were installed in the setup. Four of them were pointing towards the hydraulic jacks, allowing the staff to have a visual feedback on the displacement of the slip joint during the decommissioning steps. One camera provided an overview of the total set up to monitor the operation and a final camera captured the external part of the wind turbine tower. The total setup is schematically depicted on the right in Fig. 14.

The setup was installed in May 2019 during the preparatory decommissioning campaign. The hydraulic jacks were operating in groups of two and were powered by four individually controlled hydraulic power units (HPUs). The setting of the operating pressure p was performed manually for each HPU. The chosen pressure p relates linearly to the hydraulic jack's pushing force F_{jack} by the effective area, A_{eff}, of the pair of cylinders for each HPU. The effective area linked to each HPU was 0.014 m^2. The HPU allowed to continuously pump up to the set pressure p, to hold the instantaneous pressure and to finally release the pressure. The possible maximum value of p is equal to 700 bar per HPU, corresponding to F_{jack}=499 kN for each single hydraulic jack.

Each HPU was hereby able to control the pushing force of two hydraulic jacks in each quadrant of the slip joint, which allowed for a correction manoeuvre in any quadrant if the slip joint was found skewed during the decommissioning process. The electric shakers were controlled via one control cabinet that hosted four frequency drives to manually tune the operating frequency. The

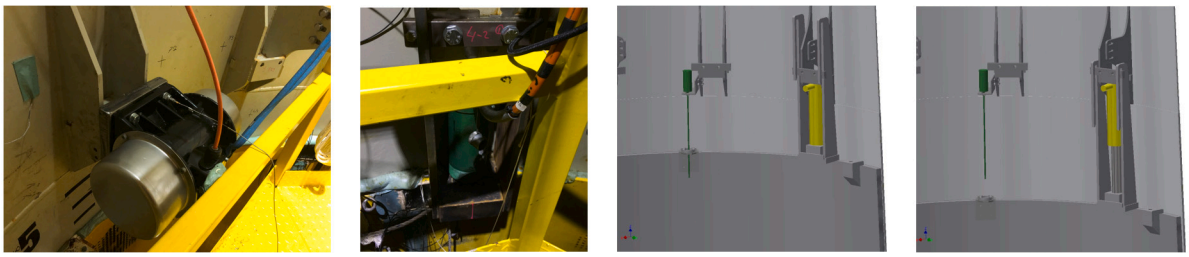

Fig. 15. Pictures of a electric shaker (left) and the hydraulic jack's working principle (right).

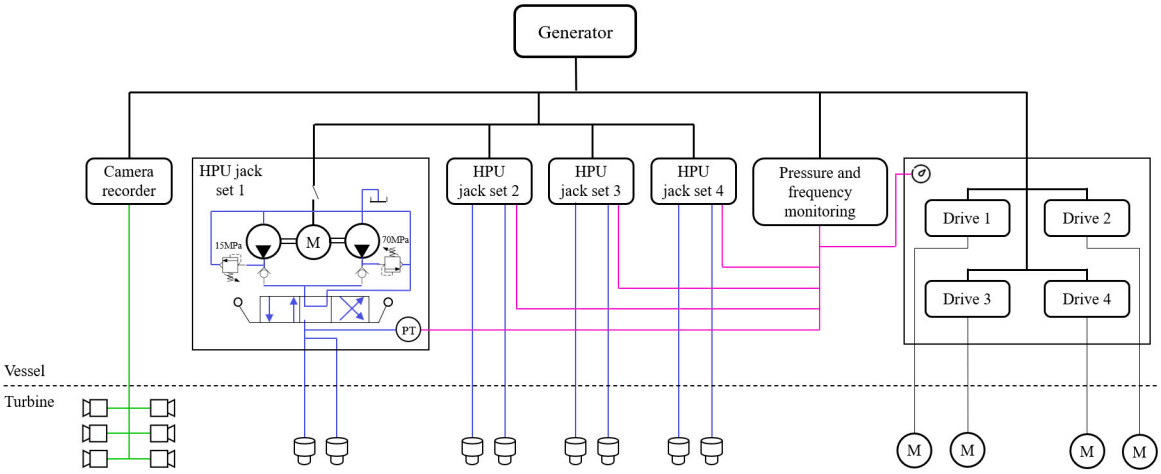

Fig. 16. Schematic of all decommissioning equipment and simplified control and communication scheme.

electric shakers could be switched on and off individually but operated all at the same chosen frequency. The pressure and frequency values were logged and the camera images were recorded. During the test in May, the video recordings were the only measurement of the slip joint's displacement, while in the actual decommissioning campaign in August four pod metres were installed at the monopile-tower interface to log the displacement with more accuracy. The whole system was powered by a stand-alone generator and was installed such that the controls were operated from the vessel. The connection between the controls on the vessel and the equipment installed on the wind turbine structure was performed through a umbilical cable. An overview of this, including a schematic diagram of the controls and communications, can be found in Fig. 16.

5.2.2. Description of the decommissioning plan

The target of the preparatory decommissioning test in May was to find the optimal combination of pushing force and oscillatory load that would initiate the disconnection of the slip joint, with the lowest possible pushing force for safety reasons. During the test, the pushing force of all hydraulic jacks F_{push} was uniformly increased. At each gradual increase, all the chosen resonance frequencies were stepped through. If at any step in the process, the slip joint would show an initial motion upwards, the corresponding combination of pushing force F_{push} and oscillation frequency f_{ex} were chosen as the optimal set of values for the actual decommissioning in August. A clear drop in pressure reading from the hydraulic jacks, combined with visual feedback from the video cameras, was taken as a sign of initial disconnection of the slip joint. An overview of this testing procedure is shown in Fig. 17. Once a first pressure drop occurred, the slip joint was pushed further up in an attempt to find a plateau pushing force. The obtained force would serve as a reasonable estimate for the expected hook load during the start of the load transfer from the jacks to the crane in the decommissioning operation. After reaching a plateau pushing force, the pressure in the hydraulic jack system was relieved to let the slip joint settle down again under the self-weight only. From this settled position, the slip joint was pushed up to the pushing force plateau and lowered down two more times in total, once with and once without the use of a vibratory load. This test was performed to confirm the obtained pushing force plateau and the reduction of the frictional force after the first disconnection. The results and observations of these tests can be found in Section 5.3.1.

The plan for the actual decommissioning executed in August was to set the hydraulic jacks and the electric shakers directly to the earlier determined combination of pushing force and oscillation frequency values to initiate the disconnection of the slip joint. As a backup, the procedure in Fig. 17 would serve as a guideline for the next steps in getting the slip joint in motion. After starting up the equipment, the slip joint would be pushed up to a distance of approximately l_{jack}=100 mm. At this point, the operation was paused to attach the rigging of the lifting vessel's crane to the wind turbine tower before restarting the pushing and dynamic loading

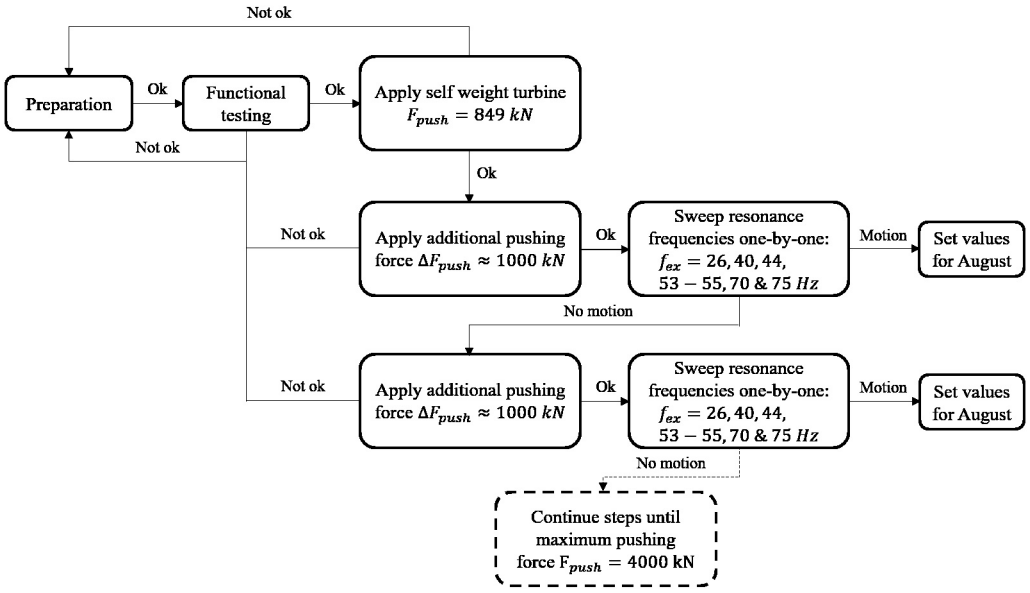

Fig. 17. Overview of testing and decommissioning procedure.

operation. When the pushing force was found below F_{push}=1080 kN, the safe threshold considering the capacity of the lifting points on the turbine, the crane initiated lifting and load transfer from the jacks to the crane was started. The electric shakers were kept on until the wind turbine tower was clearly removed from its monopile foundation to reduce the possible remaining friction to a minimum. The results and observations of this operation can be found in Section 5.3.2.

5.3. Description and observations of the decommissioning campaign

5.3.1. Preparation and test campaign May 2019

Fig. 18 shows two cycles from the first test procedure. The driving frequencies refer to the left Y-axis, while the pushing force for each HPU (with two jacks) is linked to the right Y-axis. Note that the X-axis defines a relative time, where time 0 is arbitrarily chosen at the beginning of the plot. The recorded pressure p was directly converted to a force by taking into account the A_{eff} for each HPU, while the frequency values were taken from the electric shaker drives. According to the testing procedure outlined in Fig. 17, two different levels of pushing forces are visible. For each pushing force level, the resonance frequencies were stepped through one-by-one. The occasional drop of certain frequency values was due to turning on and off some electric shakers during each test cycle in an attempt to excite the anti-nodes of each resonance mode only, in accordance with the left plot in Fig. 14.

At this stage of the testing procedure, for both pressure levels no initial movement was detected since all the pressure readings remained at their set value, which approximately corresponds to a collective pushing force of 1.9 MN and 2.8 MN, respectively. It is interesting to note that every pair of hydraulic jacks build-up plateaus at slightly different pressure levels. This is readily explained by two factors. At first, each HPU was controlled manually, causing slight offsets from the desired set point. Secondly, considering a nonaxisymmetric mass distribution of the wind turbine tower caused by the eccentricity of the rotor–nacelle–blade assembly, a slight inclination of the tower was inevitable. For ease of display, all further plots in this subsection will present only two lines. One line shows the collective pushing force, F_{push}, summing the estimated forces of all four HPU's (eight jacks), while the second line presents the average of the driving frequencies of the turned-on electric shakers.

From audible feedback during the aforementioned test, see Fig. 18, it was observed that the resonance mode around 53–55 Hz generated the loudest and most pronounced noise. Therefore, to speed up the test, a decision was made to skip the other resonance frequencies and focus on the aforementioned mode only. Fig. 19 highlights the subsequent step after the two previous cycles, where the pushing force was slightly adjusted at an amount of F_{push}=2950 kN.

Initially, the blue dashed line indicates a stable averaged pushing force. Subsequently, the red line shows the electric shakers being turned on. As soon as the driving frequency reached the desired frequency setting, 53–55 Hz, a clear decrease of the pushing force was observed. At the same time, the video recordings confirmed an initial upward displacement of the wind turbine. As mentioned above, the tower has a slight skewness because of the eccentric top mass. This small inclination caused a skewed upward motion and resulting downward motion of the tower during the testing procedure, resulting in a temporary sticking condition right before minute two of Fig. 19. The pressure in the hydraulic jacks resumed its decay right afterwards. Note that before applying an oscillatory load, the slip joint did neither show an upward displacement nor a drop of pressure. The disconnection occurred by combining the pushing force with a vibratory load. The consequent decrease of the pushing force confirms that the oscillatory force contributed to reducing the frictional stresses that used to hold the connection in place. By using Eq. (7) and mapping the measured

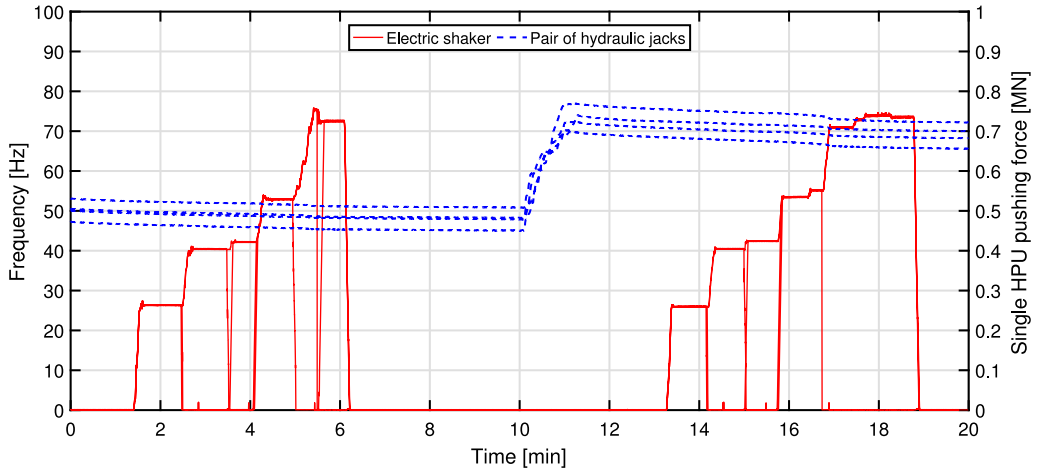

Fig. 18. Two test cycles performed in May 2019. Driving frequencies (red line) and estimated pushing forces (blue dashed line) for a pair of hydraulic jacks are displayed.

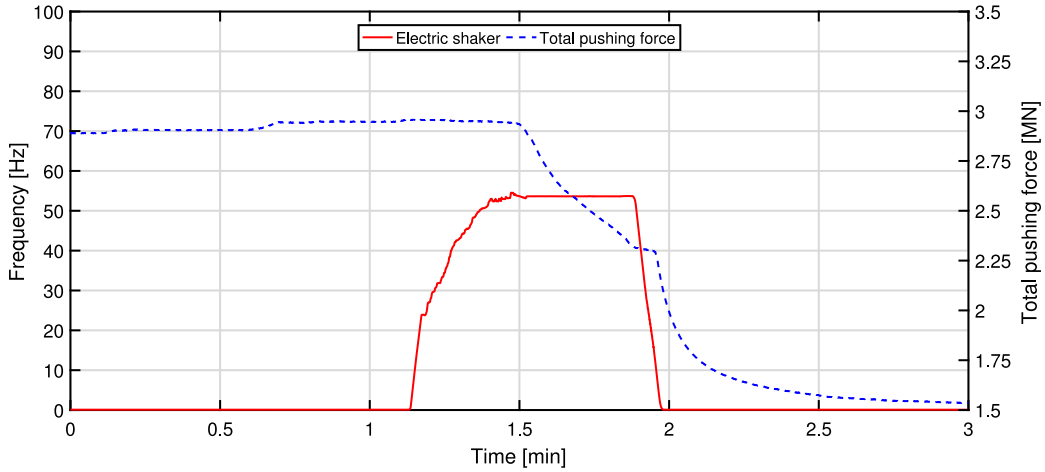

Fig. 19. Overview of a successful decommissioning attempt. The pushing force is highlighted by the blue dashed line, while the red line refers to the driving frequency.

pushing force in Fig. 12(b), it can be noticed that the pushing force would be related to a hypothetically reduced μ_s value of 0.075. The final upward movement of the lower tower section reached an amount of l_{jack}=15 mm. Fig. 19 clearly shows the effectiveness of the vibration-assisted decommissioning technique, and that friction reduction can be achieved by exciting a circumferential mode. However, it should be noted that it was not possible to quantify the amount of vibration-induced friction reduction, since a complete decommissioning test by using the pushing force only was not carried out. A test of such type would inevitably release the frictional pre-stress, biasing all further tests performed by the vibration-assisted technique.

To conclude this Section, it is worth devoting a final remark to the excited circumferential mode around 53 Hz. Assuming a hypothetical match between the mode shapes represented in Figs. 10(a) and 10(b), a possible guess for the effectiveness of exciting such mode with reference to friction reduction can be sought. According to Fig. 10(b), the mode at 53.3 Hz only refers to the dynamic of the wind turbine tower, while the monopile foundation almost acts as a rigid body. Under these circumstances, the excitation of such mode in combination with a vertical pushing force could facilitate the detachment between the two contacting surfaces. At this stage, this is only a hypothesis, and further studies are necessary in order to check whether other modes are more effective for the decommissioning purpose, especially in relation to the controllability of the whole disconnection phase and ease of excitation.

Once the slip joint was disconnected, the pressure of the hydraulic jacks showed a gradual release until an equilibrium condition between hydraulic jacks and self-weight of the structure was achieved, as shown at the very beginning of Fig. 20 where the thinner dashed blue line defines the estimated self-weight of the wind turbine tower. Subsequently, around 0.5 min, the hydraulic jacks were slightly pressurized again followed by a spontaneous release of pressure caused by the reduction in friction due to the upward movement of the slip joint. Once the pushing force reached a plateau value (see black dashed–dotted line), the HPU were set on

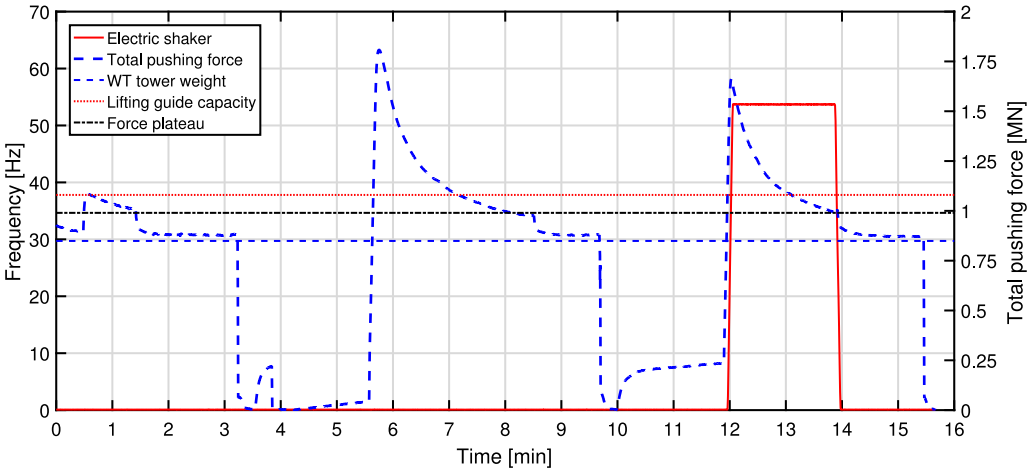

Fig. 20. Increase and release of pushing forces. The pushing force is highlighted by the blue dashed line, the red continuous line refers to the driving frequency, the red dotted line is the capacity of the lifting guide rail, the thinner blue dashed line indicates the self-weight of the wind turbine tower, while the black dashed–dotted line corresponds to the pushing force plateau value.

hold. While keeping the pressure on hold, the wind turbine tower settled itself instantaneously to find an equilibrium position, causing an additional small pressure drop that approached the self-weight of the tower. The reason for the small difference between the first pushing force plateau and the self-weight of the wind turbine tower can be explained by the skewed upward and downward motion of the wind turbine tower. Most likely, this triggered the development of a non uniform and localized contact area causing some residual friction forces to build up instantaneously after the pressure release of the hydraulic jacks.

The HPU's were switched off around minute three, allowing the slip joint to settle on the monopile tower again. Following the dashed blue line in Fig. 20, the slip joint was pushed up to l_{jack}=100 mm and subsequently allowed to settle down under its self-weight twice, once without applied vibrations (approximately around minute five in Fig. 20) and subsequently with the introduction of a vibratory load (approximately around minute twelve in Fig. 20). It can be observed that the first force build-up at the start of Fig. 20 is less pronounced compared to the two following ones. This can be explained by the fact that the starting point of Fig. 20 was right after the initial push up of l_{jack}=15 mm obtained at the end of Fig. 19, whereas the final two tests started after a complete settling phase of the slip joint on the monopile under self-weight. During this settling phase, it was assumed that friction forces could build up again. Overall, Fig. 20 shows that once most of the frictional stress was removed after the first uplift of the wind turbine tower (see Fig. 19), the pushing force tends to asymptotically approach a plateau level of 995 kN, regardless of the introduction of an applied vibratory force.

5.3.2. Actual decommissioning August 2019

The actual slip joint decommissioning was planned and executed in the night between the 15th and 16th of August 2019, using Heerema Marine Contractor's (HMC) Offshore Heavy Lift Vessel (HLV) the Aegir (see Fig. 21(a)). A dedicated control booth for all the decommissioning equipment was installed on the vessel, presented in Fig. 21(b). Additionally, an umbilical cable was also installed (see Fig. 21(c)), connecting the equipment in the control booth to the decommissioning equipment located on the wind turbine tower.

Based on the preparatory tests performed in May, the optimal values of pushing force and frequencies were F_{push}=2950 kN and 53–55 Hz, respectively. For safety reasons, the pushing force was applied in a step-wise manner up to the desired set-point. The blue dashed line in Fig. 22(a) shows the step-wise increase of the pushing force while the driving frequencies, visible in the red line, were alternatively turned on and off at 53–55 Hz.

A more general overview is presented in Fig. 22(b), in which the pushing forces and the averaged displacement from the four pod metres are displayed until the final load was transferred from the hydraulic jacks to the crane of the lifting vessel. The initial disconnection of the slip joint occurred at the peak value of the pushing force in Fig. 22(a), around 2450 kN. At the same time instant, the displacement in Fig. 22(b) clearly indicates an initial upward motion of the slip joint of about l_{jack}=75 mm. The measured maximum pushing force, is somewhat lower than the value found in May, which can well be explained by the seven month-long exposure period to environmental and wind turbine operational loads prior to the first decommissioning campaign in May 2019. This allowed the slip joint to settle further and build up more frictional stresses compared to the period preceding the decommissioning in August 2019, which was merely about three months with the absence of operational loads from the wind turbine. After the slip joint was pushed up to about l_{jack}=75 mm, the jacking operation was paused allowing the crew of the vessel to attach the rigging of the crane to the wind turbine.

With the rigging safely attached to the wind turbine, the equipment was switched on again to restart the uplifting of the slip joint. The red line in Fig. 22(b) shows the immediate continuation of the slip joint's displacement while the pushing force remains

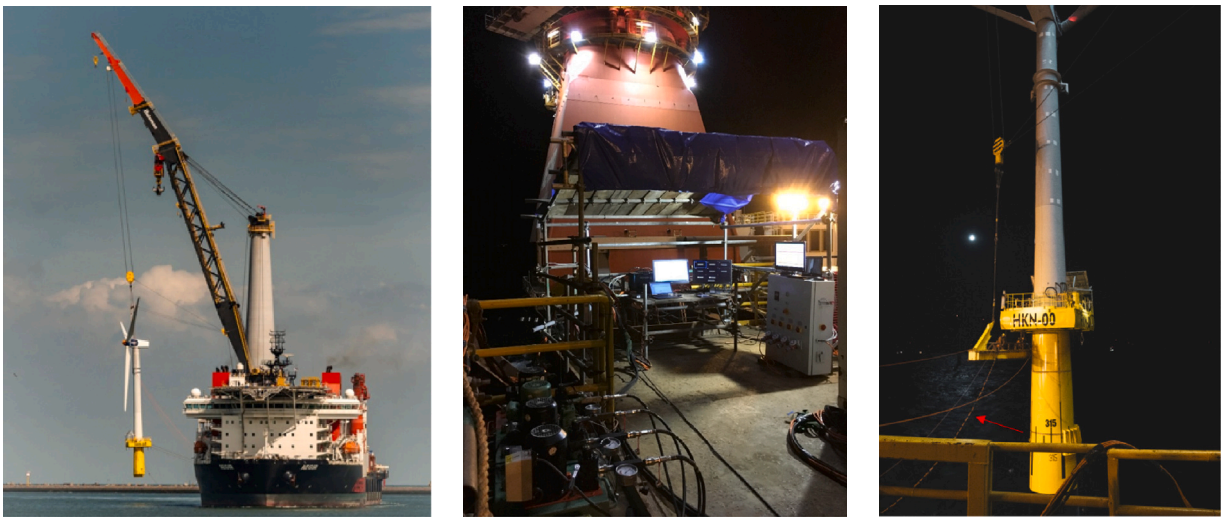

(a) HLV Aegir. (b) Control booth on HLV Aegir. (c) Umbilical installation.

Fig. 21. Pictures of DOT wind turbine decommissioning campaign in August 2019.

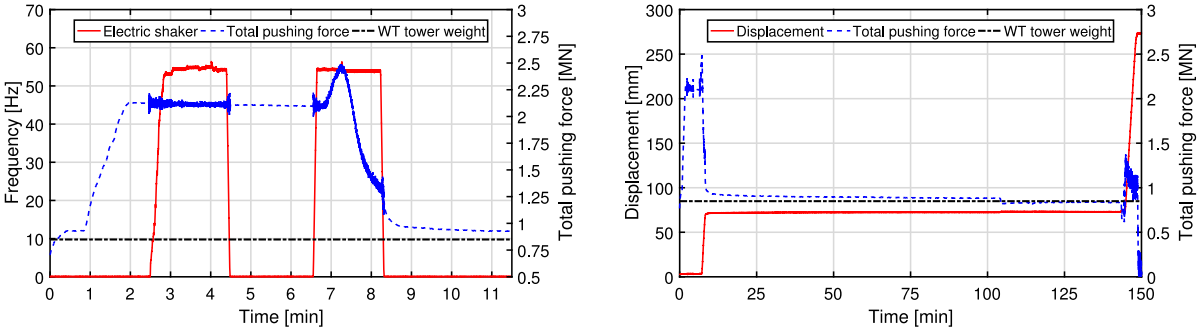

(a) Initial disconnection.

(b) Overview of the slip joint disconnection and load transfer to the crane.

Fig. 22. Decommissioning phases: (a) driving frequency and pushing force, red line and blue dashed line, respectively; (b) measured displacement and pushing force, red line and blue line, respectively. (For interpretation of the references to colour in this figure legend, the reader is referred to the web version of this article.)

at the expected plateau level discussed in the last part of Section 5.3.1. The blue dashed line in Fig. 22(b) shows a clear final drop of the pushing force from the plateau level to almost zero. After this successful phase, the crane completely took over the operation by lifting the wind turbine off its monopile support. Once the turbine was safely hanging in the crane's vessel the voyage to shore started. The wind turbine structure was then safely positioned on its temporary foundation at the quay side, ready to be decommissioned further. The readers are invited to watch an online video [37] that provides a visual and brief overview of the total operation carried out in August 2019.

6. Conclusions and future research

6.1. Conclusions

For the first time, a full-scale slip joint linking the monopile foundation and the corresponding wind turbine tower, was disconnected through a vibration-assisted decommissioning technique. This study showed the execution of the various steps necessary to complete the decommissioning procedure. As mentioned in the introduction, the key for the vibration-assisted decommissioning technique lies in the identification of the first circumferential shell modes characterizing the dynamic of the slip joint. To such regard, the experimental modal analysis of the slip joint was carried out and the local modes were identified. In order to qualitatively corroborate the experimental results, a comparative analysis with the numerical local modes extracted by a FE model was performed. The comparison showed a fairly good match in terms of the circumferential nodal pattern index N and its increase with increasing frequency. The accuracy of such a fit seems to be mainly determined by correctly modelling the geometry

and the stiffness variation between the top of the monopile and the bottom part of the wind turbine tower. The subsequent step required a possible guess of the decommissioning pushing force. In order to do so, two possible frictional regimes were assumed based on friction coefficients found in the literature. The estimates showed that the additional vertical force component generated by the frictional stresses can reach values which are from 3 times to 26 times higher than the self-weight of the wind turbine tower.

The decommissioning test setup and plan was described in Section 5.2 and a summary of the main results were shown in Section 5.3. The first decommissioning test showed that the vibration-assisted technique facilitated the slip joint disconnection by using a total pushing force of 3.5 times the self-weight of the wind-turbine tower, but still lower than the estimated ones. In particular, the slip joint detachment was triggered once the circumferential local mode at 53 Hz was excited. At this stage, after disconnecting and re-positioning the slip joint, further pushing tests showed that the further uplifting was possible by using an averaged pushing force of approximately 2.2 times higher than the self-weight of the wind turbine tower. Overall, the described decommissioning operations successfully confirmed the effectiveness of the vibration-assisted decommissioning technique.

6.2. Future research

The study conducted to plan and execute the decommissioning of the slip joint, together with the collected results, open up new research directions. Based on the results obtained so far, there is no clear evidence yet on whether or not the excitation of certain mode shapes may be more effective or sensitive than others for the decommissioning and installation phase. A previous study [19] showed that the disconnection of the slip joint was more sensitive to the excitation of specific cross-sectional mode shapes, while the stabilization of settlements during the installation phase was achieved by exciting any of the identified modes of the scaled slip joint setup. This aspect deserves a more detailed study, especially in relation to the actual developed contact area within the slip joint. The result of such study would speed up the decommissioning and eventually the installation procedure by focusing the excitation only on those modes showing the highest influence on the installation or the decommissioning phase.

The last remark is devoted to the mechanics of the slip joint. A more detailed numerical model is going to be developed to assess the contact development of the connection and identify which factors, and their corresponding sensitivity, cause a non-uniform and undesired contact area distribution over the slip joint. The numerical model will also be extended to tackle fretting and fatigue analysis by improving slip and stress predictions. Besides a more refined modelling of the contact area development, a parameter that may help to improve stress and slip predictions is the tangential interfacial contact stiffness, which allows the softening and relaxation of the contact and the occurrence of micro-slip phenomena. The identification of such parameter is not straightforward, and its physical derivation is still a challenging task within the contact mechanics research community. It is worth mentioning at this stage that the data obtained from the slip joint monitoring did not allow to identify or guess a reasonable value of such quantity, therefore laboratory experiments on a scaled slip joint are still required to propose an identification procedure for such modelling parameter.

Declaration of competing interest

The authors declare that they have no known competing financial interests or personal relationships that could have appeared to influence the work reported in this paper.

Acknowledgements

The work was part of the Slip Joint Offshore Research project, Netherland (ref. TEHE116334-SJOR) and of the Slip Joint Offshore Qualification project, Netherland (ref. TEHE117056-SJOQ), partially funded by the Dutch government, Netherland. The authors would like to thank two industrial partners of both projects, VanOord and 24SEA, for the constructive discussions during the projects and for sharing the experimental data. A further acknowledgement goes to the DOT SJOR team and Olmo Middeldorp, who assisted during the decommissioning campaign and post-processed part of the decommissioning test data, respectively.

References

[1] de Vries E. Offshore monopile failure—a solution may be in sight, Wind Power Monthly magazine. 2010, URL: https://www.windpowermonthly.com/article/1011507.

[2] NoordzeeWind. Operations Report 2009. Technical Report, NoordzeeWind; 2009, URL: http://www.noordzeewind.nl/wp-content/uploads/2012/02/OWEZ_R_000_20101112_Operations_2009.pdf.

[3] Dallyn P, El-Hamalawi A, Palmeri A, Knight R. Experimental testing of grouted connections for offshore substructures: A critical review. Structures 2015;3:90–108. http://dx.doi.org/10.1016/j.istruc.2015.03.005.

[4] Dallyn P, El-Hamalawi A, Palmeri A, Knight R. Experimental investigation on the development of wear in grouted connections for offshore wind turbine generators. Eng Struct 2016;113:89–102. http://dx.doi.org/10.1016/j.engstruct.2015.11.028.

[5] Lee J-H, Won D-H, Jeong Y-J, Kim S-H, Kang Y-J. Interfacial shear behavior of a high-strength pile to sleeve grouted connection. Eng Struct 2017;151:704–23. http://dx.doi.org/10.1016/j.engstruct.2017.08.035.

[6] Chen T, Xia Z, Wang X, Zhao Q, Yuan G, Liu J. Experimental study on grouted connections under static lateral loading with various axial load ratios. Eng Struct 2018;176:801–11. http://dx.doi.org/10.1016/j.engstruct.2018.09.056.

[7] DNV. Joint industry project summary report from the JIP on the capacity of the grouted connections in offshore wind turbine structures. Technical Report 2010–1053, Det Norske Veritas AS; 2011a.

[8] Lotsberg I, Serednicki A, Lervik A, Bertnes H. Design of grouted connections for monopile offshore structures. Stahlbau 2012;81(9):695–704. http://dx.doi.org/10.1002/stab.201201598.

[9] Voßbeck M, Löhning T, Kelm M. Structural behaviour of grouted connections for monopile foundations of offshore wind turbines. Stahlbau 2013;82(1):55–60. http://dx.doi.org/10.1002/stab.201301652.
[10] Lotsberg I. Structural mechanics for design of grouted connections in monopile wind turbine structures. Mar Struct 2013;32:113–35. http://dx.doi.org/10.1016/j.marstruc.2013.03.001.
[11] Njomo-Wandji W, Natarajan A, Dimitrov N. Probabilistic structural assessment of conical grouted joint using numerical modelling. Ocean Eng 2018;158:232–52. http://dx.doi.org/10.1016/j.oceaneng.2018.03.089.
[12] Chen T, Wang X, Yuan G, Liu J. Fatigue bending test on grouted connections for monopile offshore wind turbines. Mar Struct 2018;60:52–71. http://dx.doi.org/10.1016/j.marstruc.2018.03.005.
[13] Tziavos N, Hemida H, Metje N, Baniotopoulos C. Non-linear finite element analysis of grouted connections for offshore monopile wind turbines. Ocean Eng 2019;171:633–45. http://dx.doi.org/10.1016/j.oceaneng.2018.11.005.
[14] Jensen KS, Petersen SJ, Pedersen RR. European offshore wind engineering—past, present and future. Proc Inst Civ Eng: Civ Eng 2018;171(4):159–65. http://dx.doi.org/10.1680/jcien.17.00040.
[15] Chaki S, Cornelup G, Lillamand I, Walaszek H. Combination of longitudinal and transverse ultrasonic waves for in situ control of the tightening of bolts. J Pressure Vessel Technol 2006;129:383–90. http://dx.doi.org/10.1115/1.2748821.
[16] Sah SM, Thomsen JJ, Brøns M, Fidlin A, Tcherniak D. Estimating bolt tightness using transverse natural frequencies. J Sound Vib 2018;431:137–49. http://dx.doi.org/10.1016/j.jsv.2018.05.040.
[17] SHK. Olycka med vindkraftverk i Lemnhult, Vetlanda kommun, Jönköpings län, den 24 december 2015. Technical Report RO 2017:01, Swedish Accident Investigation Authority; 2017.
[18] Lutje Schipholt B, Van Der Tempel J. The slip-joint connection—alternative connection between pile and tower. Technical Report, DOWEC; 2003.
[19] Cabboi A, Segeren M, Hendrikse H, Metrikine A. Vibration-assisted installation and decommissioning of a slip joint. Eng Struct 2020;209:109949. http://dx.doi.org/10.1016/j.engstruct.2019.109949.
[20] Kamphuis T. Design, testing and verification of the DOT500 slip joint support structure. Master thesis, Delft University of Technology; 2016, URL: http://resolver.tudelft.nl/uuid:22375c41-8627-4509-bf94-5da3559d1002.
[21] Kamphuis T. DOT500 SLJ–TSE HER 2016–TEHE115072–Eindrapportage - v14. 2016, URL: https://projecten.topsectorenergie.nl/projecten/dot-500-inshore-tests-phase-2-00027463.
[22] Van Der Tempel J, Metrikine A. Slipjoint seafastening. NL Patent 2023699, ongoing application filed in 2019.
[23] Blekhman II. Vibrational Mechanics—Nonlinear Dynamic Effects, General Approach, Applications. Singaopre: World Scientific; 2000.
[24] Fridman HD, Levesque P. Reduction of static friction by sonic vibrations. J Appl Phys 1959;30(10):1572–5. http://dx.doi.org/10.1063/1.1735002.
[25] Godfrey D. Vibration reduces metal to metal contact and causes an apparent reduction in friction. ASLE Trans 1967;10(2):183–92. http://dx.doi.org/10.1080/05698196708972178.
[26] Tolstoi D. Significance of the normal degree of freedom and natural normal vibrations in contact friction. Wear 1967;10(3):199–213. http://dx.doi.org/10.1016/0043-1648(67)90004-X.
[27] Hess DP, Soom A. Normal vibrations and friction under harmonic loads: Part I—Hertzian contacts. J Tribol 1991;113(1):80–6. http://dx.doi.org/10.1115/1.2920607.
[28] Hess DP, Soom A. Normal vibrations and friction under harmonic loads: Part II—Rough planar contacts. J Tribol 1991;113(1):87–92. http://dx.doi.org/10.1115/1.2920608.
[29] Hess DP, Soom A, Kim C. Normal vibrations and friction at a hertzian contact under random excitation: Theory and experiments. J Sound Vib 1992;153(3):491–508. http://dx.doi.org/10.1016/0022-460X(92)90378-B.
[30] Johnson KL. Contact Mechanics. Cambridge, UK: Cambridge University Press; 1985.
[31] Tworzydlo W, Becker E. Influence of forced vibrations on the static coefficient of friction—numerical modeling. Wear 1991;143(1):175–96. http://dx.doi.org/10.1016/0043-1648(91)90093-A.
[32] Oden JT, Martins JAC. Models and computational methods for dynamic friction phenomena. Comput Methods Appl Mech Engrg 1985;52(1–3):527–634. http://dx.doi.org/10.1016/0045-7825(85)90009-X.
[33] Wetter R, Popov VL. The influence of system dynamics on the frictional resistance: Insights from a discrete model. Tribol Lett 2016;61(2). http://dx.doi.org/10.1007/s11249-015-0635-x.
[34] Chowdhury MA, Helali M. The effect of frequency of vibration and humidity on the coefficient of friction. Tribol Int 2006;39(9):958–62. http://dx.doi.org/10.1016/j.triboint.2005.10.002.
[35] Chowdhury MA, Helali M. The effect of amplitude of vibration on the coefficient of friction for different materials. Tribol Int 2008;41(4):307–14. http://dx.doi.org/10.1016/j.triboint.2007.08.005.
[36] Teidelt E, Starcevic J, Popov VL. Influence of ultrasonic oscillation on static and sliding friction. Tribol Lett 2012;48(1):51–62. http://dx.doi.org/10.1007/s11249-012-9937-4.
[37] DOT. DOT Slip joint wind turbine removal. 2020, URL: https://youtu.be/onWC6bgCSGY/.
[38] Timoshenko S, Woinowsky-Krieger S. Theory of Plates and Shells. second ed. Singapore: McGraw-Hill; 1959.
[39] DNV-GL. Fabrication and testing of offshore structures. Offshore Standard DNVGL-OS-C401, Det Norske Veritas AS; 2014.
[40] Smith M. ABAQUS/Standard User's Manual, Version 6.14. United States: Dassault Systèmes Simulia Corp; 2014.
[41] Konyukhov A, Izi R. Introduction to Computational Contact Mechanics: A Geometrical Approach. first ed. Chichester, England: John Wiley & Sons Ltd; 2015.
[42] Boulbes RJ. Troubleshooting Finite–Element Modeling with Abaqus. first ed. Cham, Switzerland: Springer Nature; 2020.
[43] Cantieni R. Experimental methods used in system identification of civil engineering structures, in: Proc. of the 1st Int. Operational Modal Analysis Conf. (IOMAC), Copenaghen, Denmark, 2005.
[44] Ewins DJ. Modal Testing: Theory, Practice, and Application. second ed. Baldock, Hertfordshire, England; 2000.
[45] Juang JN, Pappa RS. An eigensystem realization algorithm for modal parameter identification and model reduction. J Guid Control Dyn 1985;8(5):620–7. http://dx.doi.org/10.2514/3.20031.
[46] Cabboi A, Magalhães F, Gentile C, Cunha Á. Automated modal identification and tracking: Application to an iron arch bridge. Struct Control Health Monit 2017;24(1):e1854. http://dx.doi.org/10.1002/stc.1854.
[47] Shih C, Tsuei Y, Allemang R, Brown D. A frequency domain global parameter estimation method for multiple reference frequency response measurements. Mech Syst Sig Process 1988;2(4):349–65. http://dx.doi.org/10.1016/0888-3270(88)90059-3.
[48] Allaei D, Soedel W, Yang T. Natural frequencies and modes of rings that deviate from perfect axisymmetry. J Sound Vib 1986;111(1):9–27. http://dx.doi.org/10.1016/S0022-460X(86)81419-5.
[49] Fox C. A simple theory for the analysis and correction of frequency splitting in slightly imperfect rings. J Sound Vib 1990;142(2):227–43. http://dx.doi.org/10.1016/0022-460X(90)90554-D.
[50] Rabinowicz E. Friction and Wear of Materials. second ed. New York: John Wiley and Sons; 1995.
[51] Blau PJ. Friction Science and Tecnology: From Concepts to Applications. second ed. Boca Raton, USA: CRC Press, Taylor and Francis; 2009.
[52] López-Ortega A, Bayón R, Arana J. Evaluation of protective coatings for offshore applications. Corrosion and tribocorrosion behavior in synthetic seawater. Surf Coat Technol 2018;349:1083–97. http://dx.doi.org/10.1016/j.surfcoat.2018.06.089.

[53] Paslay P, Plunkett R. Design of shrink-fits. Trans ASME 1953;75:1199–202.
[54] Nolle H, Richardson R. Static friction coefficients for mechanical and structural joints. Wear 1974;28(1):1–13. http://dx.doi.org/10.1016/0043-1648(74)90097-0.
[55] Booker J, Truman C. A statistical study of the coefficient of friction under different loading regimes. J Phys D: Appl Phys 2008;41(17):174003. http://dx.doi.org/10.1088/0022-3727/41/17/174003.
[56] Booker J, Truman C. Measuring the coefficient of friction for use in shrink-fit calculations. Exp Tech 2011;35(2):7–13. http://dx.doi.org/10.1111/j.1747-1567.2009.00593.x.
[57] Atkinson R. A heat-transfer based method for slip joint contact area measurement. Master thesis, Delft University of Technology; 2018, URL: http://resolver.tudelft.nl/uuid:5943ec43-830a-4a0c-9506-9a9ce3a35129, file embargo until 2023-02-19.